Czech Technical University in Prague
Faculty of Nuclear Sciences and Physical Engineering

Department of Physics
Nuclear and Particle Physics

Energy dependence of hadron structure within quantum chromodynamics

RESEARCH THESIS

Author: Alexandra Ridziková
Supervisor: doc. Ing. Jan Čepila, Ph.D.
Year: 2023

FAKULTA JADERNÁ A FYZIKÁLNĚ INŽENÝRSKÁ
KATEDRA FYZIKY

VÝZKUMNÝ ÚKOL

Akademický rok: 2022/2023

Student: Bc. Alexandra Ridziková

Studijní program: Jaderná a částicová fyzika

Vedoucí úkolu: doc. Ing. Jan Čepila, Ph.D.

Název úkolu
(česky): Energetická závislost hadronové struktury v rámci kvantové chromodynamiky

(anglicky): Energy dependence of hadron structure within quantum chromodynamics

Jazyk VÚ: Angličtina

Pokyny pro vypracování:
1) Co je kvantová chromodynamika, kvarky a gluony, partonový model, partonové distribuce v hadronu, evoluční rovnice

2) Co je partonová saturace, proč je důležité studovat tento jev a v jakých oblastech se projevuje, jak lze tento jev zahrnout do výpočtů

3) Co je model barevného dipólu, co je vlnová funkce a dipólový účinný průřez, jak lze modelovat příčnou strukturu hadronu, co je tzv. hot-spot model

4) Co je exkluzivní a disociativní produkce vektorových mesonů, jaké jsou kinematické proměnné, které proces charakterizují, jak lze spočítat účinný průřez tohoto procesu

5) Numerický výpočet účinného průřezu v hot-spot modelu pro produkci různých vektorových mesonů na protonovém terči v kinematických rozmezích plánovaných experimentů, porovnání výsledků s daty z předchozích experimentů

6) Modifikace hot-spot modelu se zahrnutím proměnné velikosti hot-spotů a/nebo velikosti protonu, aplikace hot-spot modelu na produkci vektorových mesonů na jaderném terči

Literatura:
[1] F. Halzen and A.D.Martin, Quarks and Leptons, Wiley, 2008

[2] C. Wong, Introduction to High-energy Heavy-ion Collisions, World Scientific, 1994

[3] J. L. Albacete, C. Marquet, arxiv:hep-ph/1401.4866v1

[4] J. Cepila, J. G. Contreras and J. D. Tapia Takaki, Phys. Lett. B 766, 186 (2017)

[5] D. Bendova, J. Cepila and J. G. Contreras, Phys. Rev. D 99, no.3, 034025 (2019)

Datum zadání: 20.10.2022

Datum odevzdání: 15.08.2023

Výzkumný úkol odevzdá student v elektronické podobě nahráním souboru ve formátu pdf do příslušné události v systému Indico. Vedoucí úkolu přiloží své písemné vyjádření k práci studenta s doporučením pro hodnocení.

.....	.....
garant programu	vedoucí katedry

Prohlášení

Prohlašuji, že jsem svůj Výzkumný úkol vypracovala samostatně a uvedla jsem všechnu použitou literaturu. Nemám závažný důvod proti použití tohoto školního díla ve smyslu §60 Zákona č. 121/2000 Sb., o právu autorském, o právech souvisejících s právem autorským a o změně některých zákonů (autorský zákon).

V Praze, 2023 .....

Alexandra Ridziková

Acknowledgement

I would like to express my gratitude to my supervisor doc. Jan Čepila for his patience, providing many useful explanation and valuable guidance. Further I thank to prof. Guillermo Contreras for his insightful comments and enlightening discussions. I also thank to Matěj Vaculčiak and Dagmar Bendová for their generous assistance and help with technical issues of my work.

Alexandra Ridziková

Title:
Energy dependence of hadron structure within quantum chromodynamics

Author: Alexandra Ridziková

Type of work: Research thesis

Supervisor: doc. Ing. Jan Čepila, Ph.D.
Department of Physics, Faculty of Nuclear Sciences and Physical Engineering, Czech Technical University in Prague

Abstract: The aim of this work was to perform calculations using the Hot-spot model. This model, based on color dipole approach, provides a description of the proton structure in the transverse plane by hot spots. Hot spots are localized regions of higher partonic densities, whose positions change event-by-event. The number of hot spots increases with decreasing Bjorken-x. Moreover, the effects of making the radius of the proton and radius of hot spots energy dependent are studied. Using the Hot-spot model a cross section for exclusive and dissociative processes of vector meson production were calculated. These results were then compared to available experimental data.

Key words: deep inelastic scattering, Hot-spot model, vector meson production

Název práce:
Energetická závislost hadronové struktury v rámci kvantové chromodynamiky

Autor: Alexandra Ridziková

Abstrakt: Cílem této práce bylo provést výpočty užitím Hot-spot modelu, který v přiblížení barevného dipólu popisuje strukturu protonu v příčné rovině pomocí tzv. hot spotů. Hot spoty jsou lokalizované oblasti s vyšší partonovou hustotou, jejichž umístění se pro každou událost mění. Počet hot spotů narůstá s klesajícím Bjorkenovým-x. Současně se práce věnuje studiu vlivu změny poloměru protonu a hot spotů v závislosti na energii. S využitím zmíněného Hot-spot modelu byly spočítány účinné průřezy pro exkluzivní a disociativní procesy produkce vektorových mezonů. Tyto výsledky byly následně porovnány s dostupnými experimentálními daty.

Klíčová slovas: hluboce nepružný rozptyl, Hot-spot model, produkce vektorových mezonů

Contents

Introduction **11**

1 Phenomenology of collisions at high energies **13**
1.1 Hadron structure and the deep inelastic scattering 13
1.1.1 Deep inelastic scattering 14
1.1.2 Evolution of the partonic structure 17

2 Vector meson production within the color dipole picture **19**
2.1 Wave functions of vector meson 21
2.2 Dipole cross section 24
2.3 Hot-spot model 25
2.4 Energy dependence of parameters 26

3 Results **33**
3.1 Cross section with GBW model 33
3.2 Hot-spot model 35
3.3 Energy dependent B_p and B_{hs} 39

Conclusion **49**

Introduction

Over the past few decades, remarkable progress has been made in our understanding of the inner structure of the proton. The foundation for these studies is provided by the deep inelastic scattering (DIS) experiments in which a high-energy lepton probes the structure of a hadron. Theoretician James Bjorken predicted that the cross section for electron-proton DIS would exhibit a scaling behavior. Richard Feynman proposed that this scaling behavior indicated the presence of point-like constituents within the proton, so-called partons, which were later identified as quarks, particles whose existence can only be proven by dynamics effects.

The partonic structure of the proton is presented in terms of parton distribution functions (PDFs) that describe partonic densities as a function of longitudinal momentum fraction x of the proton carried by the parton. After the measurement of the the total fraction of the proton momentum carried by quarks, the experiments showed that this fraction was about half the total, which was the first indirect evidence for the existence of gluons, particles with no electric charge. Gluons interact with quarks, but also with themselves, which arises from the fact that gluons carry color charge. The understanding of these strong interactions between quarks and gluons, which govern the structure of hadrons like proton, is formulated by the theory of Quantum Chromodynamics (QCD).

To date, the most precise deep inelastic scattering data on the proton structure is provided by the H1 and ZEUS experiments at HERA [4]. Study of the partonic structure of the proton necessitates the use of evolution equations. These equations describe how the parton densities evolve with respect to the resolution scale Q^2 and x. At higher values of virtuality Q^2, corresponding to shorter-wavelengths of the virtual DIS photon, it is possible to resolve finer detail, which is the reason, why Q^2 is often reffered as resolution scale. Consequently, rising number of smaller quarks are "seen" in high-Q^2 deep inelastic scattering. The evolution of parton density with Q^2 is described by the Dokshitzer-Gribov-Lipatov-Altarelli-Parisi (DGLAP) evolution equations [6–9]. On the other hand, BFKL [10–12] deals with the evolution in x and a fixed scale Q^2, where the steep rise of gluons is observed at low x. However, as the gluon density rises dramatically with growing energy the solution of the BFKL equation does not correspond to some experimental data, which show less gluons, than predicted. At higher densities, the gluons in the hadron begin to overlap with each other and the nonlinear gluon recombination process becomes relevant. When this reaches a critical point, known as the saturation point, the number of gluons in a hadron is stabilized by a dynamical balance between radiation and recombination processes. There are many approaches to the study the saturation phenomena. It is provided as a solution of the non-linear

evolution equations, e.g. Balitsky-Kovchegov equation [13–15], an integro-diferencial equation with divergent kernel. A different approach relies on phenomenological modeling of the physics by using physically credible arguments for how things should work.

We will focus on the so-called Hot-spot model [30], based on the color-dipole approach. In this model, the proton configuration is represented by hot spots - localized regions of high partonic density, which change positions randomly on an event-by-event basis. The number of hot spots increases with decreasing x. This gives the proton a non-trivial internal structure that corresponds to its quantum nature. To further enhance our understanding of the dynamics of parton distributions within the proton we explore variations of this model and incorporate energy-dependent sizes of the proton and hot spots.

The thesis is organized into three main chapters. The thesis begins with an exploration of the phenomenology of collisions at high energies, focusing on the study of proton's structure. This includes a description of the deep inelastic scattering and the evolution of the partonic structure. In the second chapter, the focus shifts to vector meson production. We review the dipole picture for vector meson production and models used to calculate components of the scattering amplitude. Next we introduce the Hot-spot model and discuss its modifications. In the final chapter we present results for the cross section of exclusive and dissociative vector meson production and compare our predictions with the data.

Chapter 1

Phenomenology of collisions at high energies

1.1 Hadron structure and the deep inelastic scattering

High energy scattering experiments, in which a lepton scatters off the nucleon, have an important role in the study of the hadron structure. The process is mediated through the exchange of the virtual vector photon γ^*, radiated by the incoming lepton, with the hadron, probing its internal structure.

We will consider electron-proton scattering, here the result depends on the wavelength of the virtual photon. Elastic scattering occurs at very low energies when the wavelength of the virtual photon is large in comparison to the radius of the proton. When the wavelength of the virtual photon becomes shorter than the radius of the proton, inelastic scattering would occur. In this case, the virtual photon interacts with a constituent quark, causing the proton to break apart. With an even greater increase of energy, the wavelength of the virtual photon becomes significantly short to probe the detailed dynamic structure of the proton. The dominant process in this regime is the deep inelastic scattering. Figure 1.1 shows the nature of ep scattering depending on the wavelength of the virtual photon.

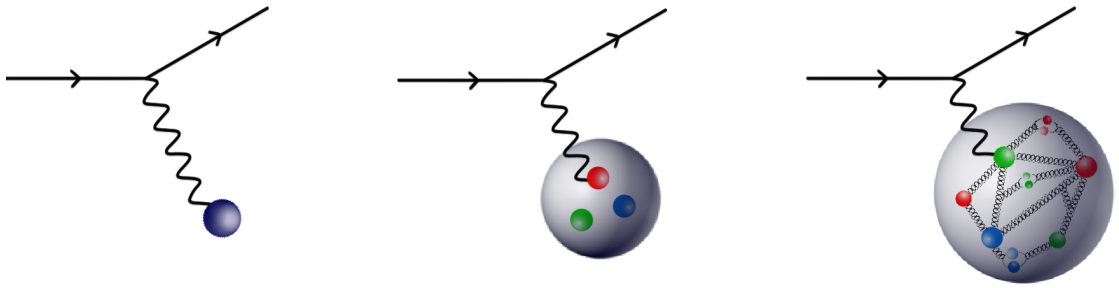

Figure 1.1: The elastic scattering (left), the inelastic scattering (middle) and the deep inelastic scattering (right).

1.1.1 Deep inelastic scattering

Let us consider the deep inelastic scattering of the electron off the proton, schematically shown in Figure 1.2. The discussion of DIS is expressed in the following kinematic notation.

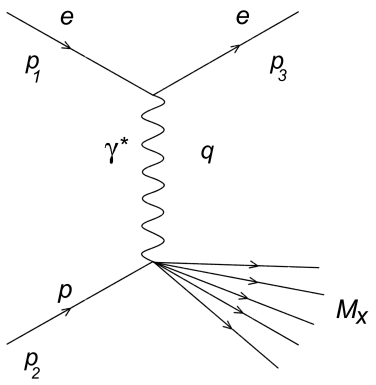

Figure 1.2: The deep inelastic scattering of the electron with the associated four-momentum p_1 off the proton with the four-momentum p_2. M_X represents the total invariant mass of outgoing particles.

The Mandelstam variable s defined as

$$s := (p_1 + p_2)^2 \tag{1.1}$$

represents the square of the center of mass (CMS) energy of the electron–proton system. One can also define the variable W^2 as

$$W^2 = (p_2 + q)^2, \tag{1.2}$$

which denotes the total energy at hadron production vertex, where

$$q = p_1 - p_3 \tag{1.3}$$

is the four-momentum of emitted virtual vector photon γ^*. As a consequence of the total four-momentum conservation, following relation must hold

$$M_X^2 = W^2 = (p_2 + q)^2 = p_2^2 + 2p_2 \cdot q + q^2, \tag{1.4}$$

where M_X represents the total invariant mass of the hadronic system.

The three quantities often used to describe the processes of DIS are the virtuality of the photon

$$Q^2 = -q^2, \tag{1.5}$$

the dimensionless Bjorken-x variable

$$x := \frac{Q^2}{2p_2 \cdot q} = \frac{Q^2}{W^2 + Q^2 - m_p^2} \tag{1.6}$$

and inelasticity

$$y := \frac{p_2 \cdot q}{p_2 \cdot p_1}. \tag{1.7}$$

Here, the mass of the proton is denoted by m_p. The virtuality Q^2 corresponds to the momentum transferred during scattering, and the scale Q^2 determines the resolution of the scattering process. The Bjorken-x is in the context of the infinite momentum frame, interpreted as the fraction of proton's longitudinal momentum carried by one of its constituents. In the high energy limit, which corresponds to $s \sim Q^2/x$, Bjorken-x decreases. The inelasticity y quantifies the fraction of the initial electron energy lost in collision. In the case of DIS the inelasticity $y \to 1$.

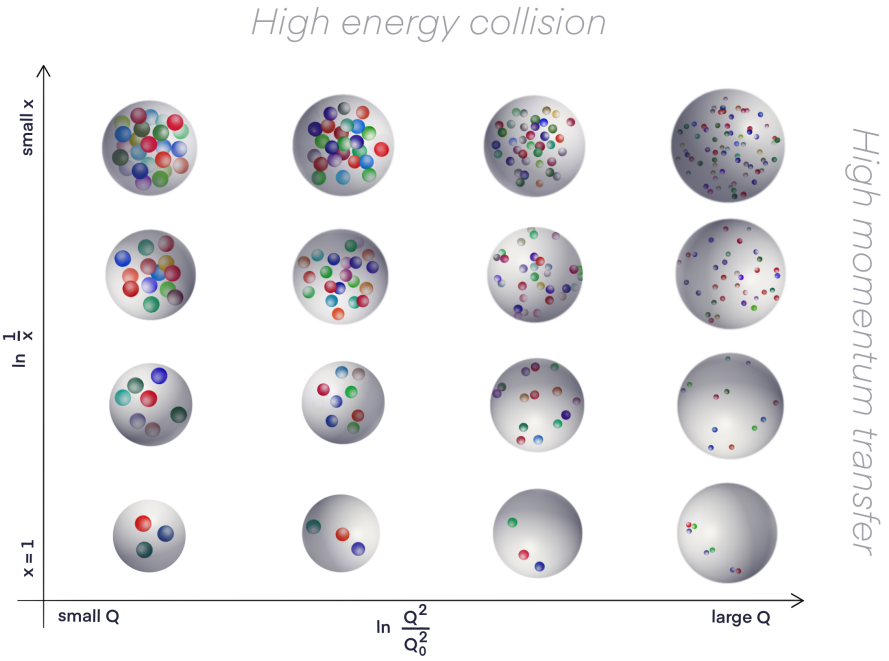

Figure 1.3: Parton density evolution. The vertical axis shows the parton density and horizontal axis represents the resolution of the probe.

Cross section and Parton model

For the deep inelastic scattering we get the following relation for differential cross section:

$$\frac{\mathrm{d}^2\sigma}{\mathrm{d}x\mathrm{d}Q^2} = \frac{4\pi\alpha_{em}^2}{Q^4}\left[(1-y)\frac{F_2(x,Q^2)}{x} + y^2 F_1(x,Q^2)\right], \tag{1.8}$$

where α_{em} is the electromagnetic coupling constant. The cross section is proportional to the combination of two structure functions $F_1(x,Q^2)$ and $F_2(x,Q^2)$, which generally depend on both Q^2 and x. However, first experimental data showed that structure functions are independent of Q^2,

$$F_1(x,Q^2) \to F_1(x) \quad \text{and} \quad F_2(x,Q^2) \to F_2(x), \tag{1.9}$$

which is called Bjorken scalling. The absence of dependence of Q^2 indicates scattering from point-like constituents. Moreover, the structure functions are not independent, but the Callan-Gross relation [1],

$$F_2(x) = 2xF_1(x), \tag{1.10}$$

holds. This observation suggests that scattering occurs on fermions with spin 1/2. Consequently, the underlying process can be interpreted as the elastic scattering of the electron off one of the partons inside the proton.

The parton model proposed by Feynman [2, 3], which is formulated in the infinite momentum frame, understands hadrons as composite objects of point-like particles (partons) each of them carries a fraction of the total proton longitudinal momentum, which corresponds to the Bjorken-x, while the transverse momenta of partons are neglected. The sum over the momenta of all partons should correspond to the total momentum of the proton. The experiments, however have revealed that quarks carry approximately half of the total momentum of the proton. The remainder is carried by the gluons, which are electrically neutral bosons.

Nevertheless, the proton is a dynamic system, where quarks are constantly exchanging gluons by strong interaction. These gluons can fluctuate into the sea quark-antiquark pairs, which tend to occur in the low-x region.

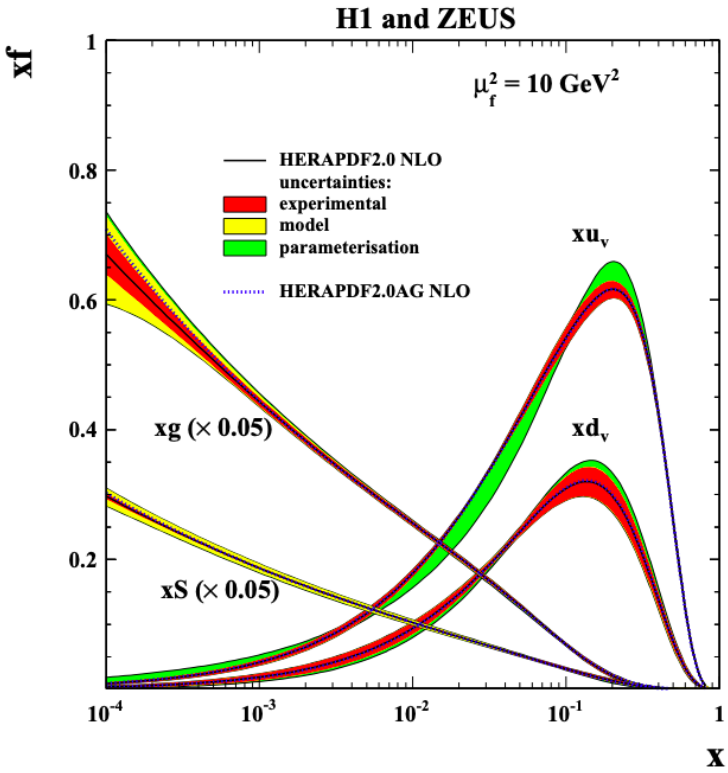

Figure 1.4: The evolution in Bjorken-x of the valence-quarks, sea-quarks and gluons distributions measured at HERA [4].

1.1.2 Evolution of the partonic structure

The investigation of parton distribution functions was carried out by the ZEUS and H1 experiments at HERA, providing information about how the structure of the proton depends on variables x and Q^2 (resolution scale). In the high-energy limit, which corresponds to small x, the density of partons increases significantly, and the partonic system is predominantly formed by gluons. At high momentum transfer and a fixed x, an observation reveals the presence of a clusters of smaller partons. The vertical direction describes the evolution of the proton structure with increasing resolution scale.

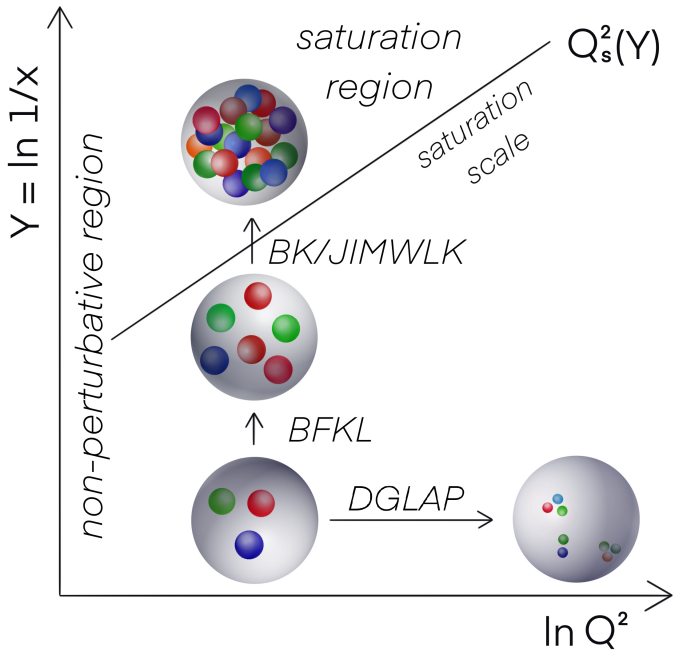

Figure 1.5: Evolution of the partonic structure of the proton and the regions of applicability of evolution equations.

DGLAP

With increasing Q^2, the number of resolved partons within the proton increases. The probability of finding a quark at high momentum fraction x is decreasing, due to the fact that high-momentum quarks lose momentum by radiating gluons [5]. The DGLAP (Dokshiter-Gribov-Lipatov-Altarelli-Parisi) [6–9] evolution equation

$$\frac{\mathrm{d}q_f(x,Q^2)}{\mathrm{d}\ln Q^2} = \frac{\alpha_S}{2\pi}\int_x^1 \frac{\mathrm{d}y}{y}\left(q_f(y,Q^2)P_{qq}\left(\frac{x}{y}\right) + g(y,Q^2)P_{qg}\left(\frac{x}{y}\right)\right), \tag{1.11}$$

$$\frac{\mathrm{d}g(x,Q^2)}{\mathrm{d}\ln Q^2} = \frac{\alpha_S}{2\pi}\int_x^1 \frac{\mathrm{d}y}{y}\left(q_f(y,Q^2)P_{gq}\left(\frac{x}{y}\right) + g(y,Q^2)P_{gg}\left(\frac{x}{y}\right)\right) \tag{1.12}$$

expresses that the quark $q_f(x,Q^2)$ with flavor f, or gluon $g(x,Q^2)$, with the momentum fraction x could have come from the parent quark $q_f(y,Q^2)$, or gluon $g(y,Q^2)$, with

momentum fraction y. The splitting functions P_{ij} capture the dynamics of parton emission and annihilation, which contribute to the evolution of parton densities within the hadron.

This splitting function P_{qq} describes the probability of a parent quark emitting a gluon, leading to a daugher quark with reduced momentum fraction by a factor of z. Similarly, the splitting function P_{gg} represents the probability of gluon emission from a parent gluon. The function P_{gq} characterizes the probability of generating a daughter gluon through the annihilation of a quark-antiquark pair and the splitting function P_{qg} corresponds to the probability of a gluon converting into a $q\bar{q}$ pair, with the quark carrying a momentum fraction z and the antiquark carrying a momentum fraction $(1-z)$.

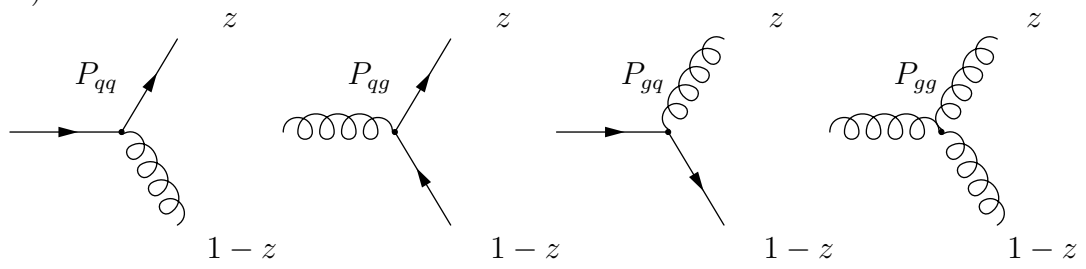

Figure 1.6: Symbolic representation of splitting functions.

Evolution with decreasing x

Having explored the evolution of parton densities with respect to resolution, we now turn our attention to the evolution with decreasing x. The BFKL evolution equation, which was suggested by Balitsky, Fadin, Kuraev and Lipatov [10–12] deals with the high energy limit (large s), which corresponds to small-x, and fixed Q^2. This equation describes the linear evolution of gluon densities as the rapidity, $Y = \ln \frac{1}{x}$, increases. According to the BFKL equation, parton densities exhibit a steep rise with decreasing x. As the solution of the BFKL equation progresses, the total cross section demonstrates exponential growth with increasing rapidity, indicating that a greater number of gluons are emitted. Consequently, the probability of further emissions increases, leading to a divergence in the cross section.

At a certain point, as parton densities evolve with $\ln \frac{1}{x}$, the proton becomes densely filled with gluons. At this stage, the probability of interaction between two gluons can no longer be overlooked, and individual partons eventually start to overlap or shadow each other. As a critical gluon density is reached, gluon wave functions begin to overlap, resulting in gluon recombination becoming as important as gluon branching, which causes the evolution of gluon densities to deviate from linearity and become nonlinear as x decreases. Consequently, the rapid growth of the gluon distribution is eventually constrained. This phenomenon, known as saturation, occurs when the dynamical balance between the gluon recombination ($gg \to g$) and the radiation ($g \to gg$) is reached. The BFKL evolution equation does not account for gluon recombination, which becomes important in the kinematic region of very small-x. To accurately describe the dynamics in this regime, nonlinear evolution equations are required. Some of the widely studied are the JIMWLK (Jalilian-Marian-IancuMcLerran-Weigert-Leonidov-Kovner) [16–19] evolution equation and BK (Balitsky-Kovchegov) [13–15] evolution equation obtained as the simplified version of JIMWLK.

Chapter 2

Vector meson production within the color dipole picture

Up to this point, we considered the infinite momentum frame. In low-x region, it is useful to consider the collision from a perspective, where the target particle (proton) is at rest. In this frame, the process of vector meson production is based on the concept of color dipoles, where the virtual photon fluctuates into a pair of quark and antiquark, each carrying a fraction of the original momentum z or $(1-z)$, respectively. The transverse size of the dipole is represented by the variable $\vec{r}$. The $q\overline{q}$ pair interacts with the target proton through the exchange of a colorless state with quantum numbers of vacuum, known as the Pomeron [20], which in the simplest approximation can be represented by two gluons, leading to various final-state particles.

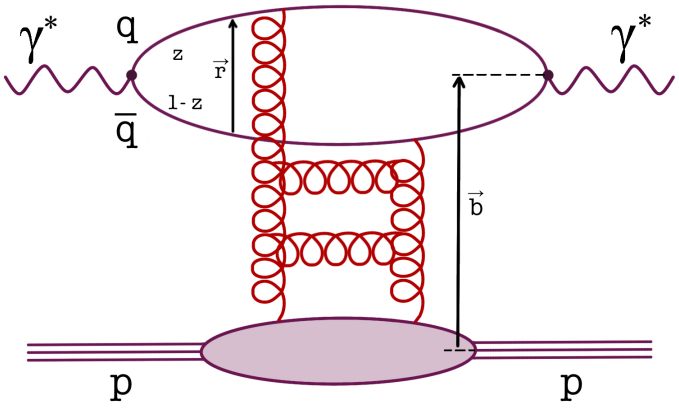

Figure 2.1: Schematic diagrams illustrating the elastic scattering in the context of the color dipole picture. Variable $\vec{r}$ represents the transverse size of the dipole and $\vec{b}$ is the impact parameter between the dipole and the target.

Exclusive vector meson production refers to the process in which the target proton remains intact, leading only to the production of a vector meson. In contrast, dissociative vector meson production involves the production of a vector meson along with a breakup of the target proton. Vector meson production can occour in both photoproduction (where $Q^2 \to 0$) and electroproduction (where $Q^2 \gtrsim 1$).

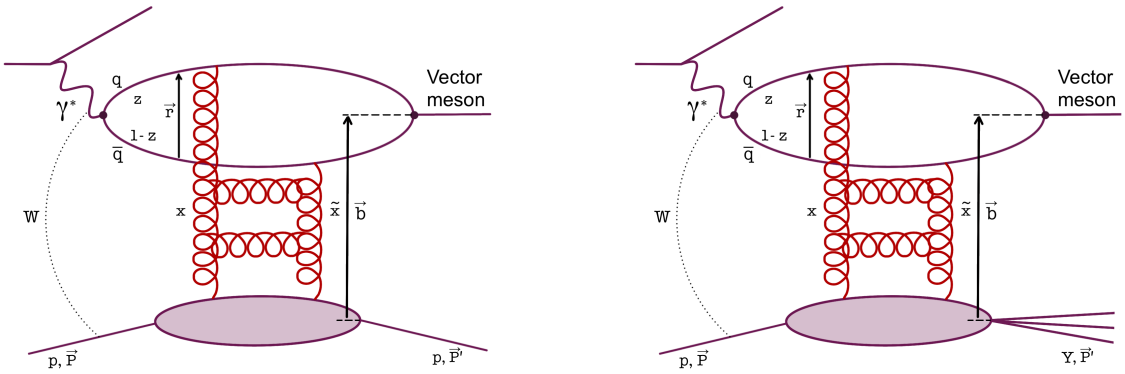

Figure 2.2: Schematic diagrams illustrating the exclusive (left) and dissociative (right) production of a vector meson.

The amplitude for the exclusive vector meson (VM) production is denoted by [21]

$$\mathcal{A}_{T,L}^{\gamma^* p \to VMp}(x, Q^2, \Delta) = i \int \mathrm{d}^2 r \int_0^1 \frac{\mathrm{d}z}{4\pi} \, |\Psi_{VM}^* \Psi_{\gamma^*}|_{T,L} \, \mathcal{A}_{q\bar{q}}(x, r, \Delta), \tag{2.1}$$

where $\mathcal{A}_{q\bar{q}}$ represents the amplitude of the dipole scattering with the target and $|\Psi_{VM}^* \Psi_{\gamma^*}|_{T,L}$ are the overlaps between the photon wave function Ψ_{γ^*} and vector meson wave function Ψ_{VM}, which describe the fluctuation of the photon into the dipole and the formation of the vector meson in the final state, respectively. In this case, the Bjorken-x takes form

$$x = \frac{M_{VM}^2 + Q^2}{W^2 + Q^2}, \tag{2.2}$$

where M_{VM} represents the invariant mass of the given vector meson and W^2 is the square of center of mass energy of the photon proton system. In order to describe the process of vector meson production, a new variable $t = (\vec{P} - \vec{P}')^2$, the square of momentum transfer in the proton vertex, is used. The transverse momentum lost by the outgoing proton, $\vec{\Delta} = \vec{P} - \vec{P}'$, is related to t through relation

$$\Delta^2 = -t. \tag{2.3}$$

The amplitude (2.1) can be formulated as [21]

$$\mathcal{A}_{T,L}^{\gamma^* p \to VMp}(x, Q^2, \Delta) = i \int \mathrm{d}^2 r \int_0^1 \frac{\mathrm{d}z}{4\pi} \int \mathrm{d}^2 b \, |\Psi_{VM}^* \Psi_{\gamma^*}|_{T,L} \, e^{-i[\vec{b} - (1-z)\vec{r}]\vec{\Delta}} \, \frac{\mathrm{d}\sigma_{q\bar{q}}}{\mathrm{d}^2 b} \tag{2.4}$$

with $\vec{b}$ being the impact parameter between the proton and the dipole, variable $\vec{r}$ represent the dipole transverse radius and $\vec{z}$ the momentum fraction of the photon carried by a quark. Furthermore, the information about the interaction between a color dipole and the proton is encoded in the differential $q\bar{q} - p$ cross section $\mathrm{d}\sigma_{q\bar{q}}/\mathrm{d}^2 b$.

Using Bessel functions of the first kind (J_0), and further, by using the spherical symmetry of the proton, the amplitude reduces to

$$\mathcal{A}_{T,L}^{\gamma^* p \to VMp} = i \int_0^\infty \mathrm{d}r 2\pi r \int_0^1 \frac{\mathrm{d}z}{4\pi} \int_0^\infty \mathrm{d}b 2\pi b |\Psi_{VM}^* \Psi_{\gamma^*}|_{T,L} J_0(b\Delta) J_0[(1-z)r\Delta] \frac{\mathrm{d}\sigma_{q\bar{q}}}{\mathrm{d}^2 b}. \tag{2.5}$$

In order to calculate the amplitude, the the wave function and the color dipole cross section need to be modeled. These components will be discussed in the following sections.

In the color dipole picture, the differential cross section for the exclusive vector meson production is given by

$$\frac{\mathrm{d}\sigma_{T,L}^{\gamma^* p\to VMp}}{\mathrm{d}|t|} = \frac{\left(1+\beta_{T,L}^2\right)\left(R_g^{T,L}\right)^2}{16\pi}\left|\mathcal{A}_{T,L}^{\gamma^* p\to VMp}\right|^2, \tag{2.6}$$

where the factor $\left(1+\beta_{T,L}^2\right)$ accounts for the contribution from the real part of the amplitude [21]. $\beta_{T,L}$ is calculated as

$$\beta_{T,L} = \tan(\pi\lambda_{T,L}/2), \quad \text{where} \quad \lambda_{T,L} = \frac{\partial \ln\left(\mathcal{A}_{T,L}^{\gamma^* p\to VMp}\right)}{\partial \ln \frac{1}{x}}. \tag{2.7}$$

The second factor

$$R_g^{T,L} = \frac{2^{2\lambda_{T,L}+3}}{\sqrt{\pi}}\frac{\Gamma(\lambda_{T,L}+\frac{5}{2})}{\Gamma(\lambda_{T,L}+4)} \tag{2.8}$$

represents the *skewedness correction* [22], which addresses the presence of two distinct values of x in the interaction while only one appears in equation (2.5). The resulting differential cross section is given by the sum of the transverse and longitudinal contributions:

$$\frac{\mathrm{d}\sigma^{\gamma^* p\to VMp}}{\mathrm{d}|t|} = \frac{1}{16\pi}\Big(\left(1+\beta_T^2\right)\left(R_g^T\right)^2\left|\mathcal{A}_T^{\gamma^* p\to VMp}\right|^2 + \left(1+\beta_L^2\right)\left(R_g^L\right)^2\left|\mathcal{A}_L^{\gamma^* p\to VMp}\right|^2\Big). \tag{2.9}$$

The integral of the differential cross section over t, in the range given by the experimental data, gives the total cross section

$$\sigma(x,Q^2) = \int_0^{t_{max}} \mathrm{d}|t|\frac{\mathrm{d}\sigma}{\mathrm{d}|t|}. \tag{2.10}$$

2.1 Wave functions of vector meson

The modeling of the scalar part of wave functions, $\phi_{T,L}$, in vector meson production assumes that vector mesons primarily consist of a $q\overline{q}$ pair with a polarization structure identical to that of a photon. The overlaps between the photon-meson wave functions are given as [21]

$$|\Psi_{VM}^*\Psi_{\gamma^*}|_T = \hat{e}_f e\frac{N_c}{\pi z(1-z)}\left[m_f^2 K_0(\epsilon r)\phi_T(r,z) - [z^2+(1-z)^2]\epsilon K_1(\epsilon r)\partial_r\phi_T(r,z)\right], \tag{2.11}$$

$$|\Psi_{VM}^*\Psi_{\gamma^*}|_L = \hat{e}_f e\frac{N_c}{\pi}2Qz(1-z)K_0(\epsilon r)\left[M_{VM}\phi_L(r,z) + \delta\frac{m_f^2-\nabla_r^2}{M_{VM}z(1-z)}\phi_L(r,z)\right], \tag{2.12}$$

where $e = \sqrt{4\pi\alpha_{em}}$, and $N_c = 3$ is the number of colors. The effective charge of given vector meson is represented by $\hat{e}_f = \frac{2}{3}$, $\frac{1}{3}$, $\frac{1}{3}$, and $\frac{1}{\sqrt{2}}$ for the J/ψ, $\Upsilon(1S)$, ϕ and ρ meson, respectively. The M_{VM} is the invariant mass of vector meson and m_f is the mass of the quark of flavor f. $K_{0,1}$ are the Bessel functions of the second kind, $\epsilon^2 = z(1-z)Q^2 + m_f^2$ and $\partial_r K_0(\epsilon r) = -\epsilon K_1(\epsilon r)$. ∇_r^2 denotes the Laplace operator.

The scalar part $\phi_{T,L}$ of the wave function depends on the model used. In this work, two models are used, "Gaus-LC" [23] and "boosted Gaussian" [24–26]. In the Gaus-LC model, the parameter δ used in (2.12) is set to $\delta = 0$. The scalar parts of the wave function are defined as

$$\phi_T(r,z) = N_T(z(1-z))^2 \exp\left(-\frac{r^2}{2R_T^2}\right), \tag{2.13}$$

$$\phi_L(r,z) = N_L z(1-z) \exp\left(-\frac{r^2}{2R_L^2}\right). \tag{2.14}$$

The values of the constants $N_{T,L}$ and $R_{T,L}$ are given in Table 2.1. Therefore, the form of the overlap functions (2.11),(2.12) for Gaus-LC is

$$|\Psi_{VM}^*\Psi_{\gamma^*}|_T = \hat{e}_f e \frac{N_c}{\pi z(1-z)}\Big[m_f^2 K_0(\epsilon r)\phi_T(r,z) - [z^2+(1-z)^2]\epsilon K_1(\epsilon r)\Big(-\frac{r}{R_T^2}\Big)\phi_T(r,z)\Big],$$

$$|\Psi_{VM}^*\Psi_{\gamma^*}|_L = \hat{e}_f e \frac{N_c}{\pi} 2Qz(1-z)K_0(\epsilon r) M_{VM}\phi_L(r,z).$$

The following model is boosted Gaussian in which the scalar parts are given as

$$\phi_{T,L}(r,z) = \mathcal{N}_{T,L} z(1-z) \exp\Big(-\frac{m_f^2\mathcal{R}^2}{8z(1-z)} - \frac{2z(1-z)r^2}{\mathcal{R}^2} + \frac{m_f^2\mathcal{R}^2}{2}\Big). \tag{2.15}$$

In the boosted Gaussian case, the parameter $\delta = 1$, hence the overlap functions (2.11), (2.12) can be rewritten as

$$\begin{aligned}|\Psi_{VM}^*\Psi_{\gamma^*}|_T =& \hat{e}_f e \frac{N_c}{\pi z(1-z)}\phi_T(r,z)\cdot \\ &\cdot\left[m_f^2 K_0(\epsilon r) - [z^2+(1-z)^2]\epsilon K_1(\epsilon r)\left(-\frac{4z(1-z)r}{\mathcal{R}^2}\right)\right],\end{aligned}$$

$$\begin{aligned}|\Psi_{VM}^*\Psi_{\gamma^*}|_L =& \hat{e}_f e \frac{N_c}{\pi} 2Qz(1-z)K_0(\epsilon r)\phi_L(r,z)\cdot \\ &\cdot\left[M_{VM} + \frac{m_f^2}{M_{VM}z(1-z)} + \frac{8(\mathcal{R}^2 - 2z(1-z)r^2)}{\mathcal{R}^4 M_{VM}}\right]\end{aligned}$$

with parameters $\mathcal{N}_{T,L}$ and $\mathcal{R}$ given in Table 2.2.

	M_V [GeV]	m_f [GeV]	N_T	R_T^2 [GeV^{-2}]	N_L	R_L^2 [GeV^{-2}]
J/ψ	3.097	1.4	1.23	6.5	0.83	3.0
ϕ	1.019	0.14	4.75	16.0	1.41	9.7
ρ	0.776	0.14	4.47	21.9	1.79	10.4

Table 2.1: Parameters of the *Gaus-LC* model for vector meson wave functions [21].

	M_V [GeV]	m_f [GeV]	$\mathcal{N}_T$	$\mathcal{N}_L$	$\mathcal{R}^2$ [GeV^{-2}]
J/ψ	3.097	1.4	0.578	0.575	2.3
ϕ	1.019	0.14	0.919	0.825	11.2
ρ	0.776	0.14	0.911	0.853	12.9
$\Upsilon(1S)$	9.460	4.2	0.478	0.478	0.585

Table 2.2: Parameters of the *boosted Gaussian* model for vector meson wave functions [21], [32].

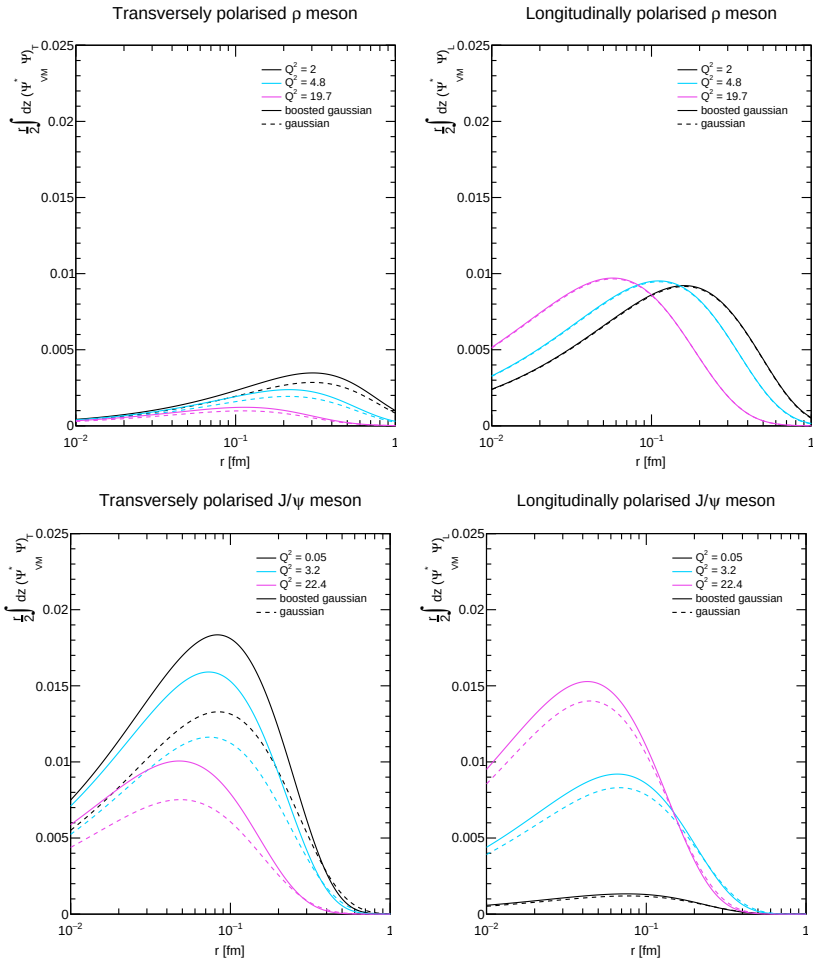

Figure 2.3: The overlap functions between the vector meson and photon wave function integrated over z for different values of Q^2.

2.2 Dipole cross section

The dipole-proton cross section can be obtained from the imaginary part of the dipole-proton amplitude $N(x, \vec{r}, \vec{b})$ using the optical theorem [21]:

$$\frac{\mathrm{d}\sigma_{q\bar{q}}}{\mathrm{d}\vec{b}} = 2N(x, \vec{r}, \vec{b}). \tag{2.16}$$

The factorized form of the dipole cross section, given by

$$\frac{\mathrm{d}\sigma_{q\bar{q}}}{\mathrm{d}\vec{b}} = \sigma_0 N(x, r) T_p(\vec{b}) \tag{2.17}$$

involves the proton profile function $T_p(\vec{b})$, which describes the proton profile in the impact parameter plane. This factorization, which was proposed in [29], allows the separation of contributions arising from fluctuations in the proton structure and the energy dependence of the cross section. The term σ_0 represents a normalization factor, which is fixed in this work to $\sigma_0 = 4\pi B_p$. The parameter B_p may be interpreted as the average of the squared transverse radius of the proton and will be further discussed in following sections. It is crucial to note that the use of the factorized form of the dipole cross section with the proton profile function is model-dependent and does not hold universally.

GBW parameterization

The dipole amplitude can be obtained using various parameterizations. One of the well-known example is the model proposed by Golec-Biernat and Wüsthoff [27, 28]:

$$N(x, r) = \left[1 - \exp\left(-\frac{r^2 Q_s^2(x)}{4}\right)\right] \tag{2.18}$$

with $Q_s(x)$ being the saturation scale,

$$Q_s^2(x) = Q_0^2 \left(\frac{x_0}{x}\right)^{\lambda} \ [\mathrm{GeV}^2], \tag{2.19}$$

where Q_0^2 is parameter, which is set to 1 GeV^2. The exponent λ characterizes the growth of the dipole cross section with decreasing x, indicating the rapid increase of parton densities in the high-energy regime. The term x_0 is a free parameter, listed in Table 2.4.

Proton profile function

Various prescriptions for proton profile functions $T_p(b)$ can be used to parameterize the gluon density within the proton. In this work we use a Gaussian distribution and a set of random fluctuations to describe the proton transverse profile.

Gaussian distribution

$$T_p(b) = \frac{1}{2\pi B_p} e^{-\frac{b^2}{2B_p}}, \tag{2.20}$$

describes the exponential fall-off of parton density as a function of transverse distance from the proton center.

Integration of the differential dipole cross section over the impact parameter, gives the expression

$$\sigma_{q\bar{q}} = \int \mathrm{d}^2 b \sigma_0 N(x,r) T_p(b) = \sigma_0 N(x,r), \tag{2.21}$$

where the normalization condition

$$\int \mathrm{d}^2 b \; T_p(b) = 1 \tag{2.22}$$

has been applied.

Hence, the amplitude (2.5) can be written as

$$\mathcal{A}_{T,L}^{\gamma^* p \to VMp} = iA_b \cdot (A_r)_{T,L} \tag{2.23}$$

where

$$A_b = \int_0^\infty \mathrm{d}b \, 2\pi b J_0(b\Delta) T_p(b), \tag{2.24}$$

$$(A_r)_{T,L} = \sigma_0 \int_0^\infty \mathrm{d}r \, 2\pi r N(x,r) (A_z)_{T,L}, \tag{2.25}$$

$$(A_z)_{T,L} = \int_0^1 \frac{\mathrm{d}z}{4\pi} \, |\Psi_{VM}^* \Psi_{\gamma^*}|_{T.L} J_0((1-z)r\Delta). \tag{2.26}$$

2.3 Hot-spot model

Due to the quantum nature of the proton, its structure changes from interaction to interaction. According to this model, which was used in [30] to study the photoproduction of J/ψ, the parton distribution within the proton is not uniform, but exhibits localized regions of higher parton densities, known as hot spots. The number of hot spots at random positions b_j is denoted by N_{hs}, and each hot spot follows a Gaussian distribution

$$T_{hs}(\vec{b} - \vec{b_j}) = \frac{1}{2\pi B_{hs}} e^{-\frac{(\vec{b}-\vec{b_j})^2}{2B_{hs}}} \tag{2.27}$$

characterized by a width B_{hs}, which can be interpreted as an average of the squared radius of the hot spot. The proton profile is then given by

$$T_p(\vec{b}) = \frac{1}{N_{hs}} \sum_{j=1}^{N_{hs}} T_{hs}(\vec{b} - \vec{b_j}). \tag{2.28}$$

Each vector $\vec{b_j}$ is sampled from a two-dimensional Gaussian distribution centered at the origin $(0,0)$ with a width B_p.

The Hot-spot model includes the indirect energy dependence of the proton profile $T_p(\vec{b})$ through the evolution of the number of hot spots depending on x. N_{hs} is then a randomly generated integer value from the zero-truncated Poisson distribution, with Poisson distribution mean value being

$$\langle N_{hs}(x)\rangle = p_0 x^{p_1}(1 + p_2\sqrt{x}), \tag{2.29}$$

where p_0, p_1 and p_2 are parameters listed in Table 2.5. This reflects the concept that at a given fixed scale, the number of hot spots increases with increasing energy.

By combining all the components and utilizing the analytical evaluation of certain integrals [31], the amplitude can be expressed as follows:

$$\mathcal{A}_{T,L} = iA_b \cdot (A_r)_{T,L}, \tag{2.30}$$

with

$$A_b = \int \mathrm{d}\vec{b} e^{-i\vec{b}\cdot\vec{\Delta}} T(\vec{b}) = e^{\left(-\frac{B_{hs}\Delta^2}{2}\right)} \frac{1}{N_{hs}} \sum_{j=1}^{N_{hs}} e^{-i\vec{b_j}\cdot\vec{\Delta}}, \tag{2.31}$$

$$(A_r)_{T,L} = \sigma_0 \int \mathrm{d}r 2\pi r \int_0^1 \frac{\mathrm{d}z}{4\pi} \left|\Psi^*_{VM}\Psi_{\gamma^*}\right|_{T,L} J_0((1-z)r\Delta) N(x,r). \tag{2.32}$$

The cross section for the exclusive process is then given by

$$\frac{\mathrm{d}\sigma^{\gamma^* p\to VMp}_{T,L}}{\mathrm{d}|t|} = \frac{\left(R_g^{T,L}\right)^2}{16\pi} \left|\langle \mathcal{A}_{T,L}\rangle\right|^2 \tag{2.33}$$

and the cross section for the dissociative process where, the proton dissociates into a system Y is

$$\frac{\mathrm{d}\sigma^{\gamma^* p\to VMY}_{T,L}}{\mathrm{d}|t|} = \frac{\left(R_g^{T,L}\right)^2}{16\pi} \left(\langle|\mathcal{A}_{T,L}|^2\rangle - |\langle \mathcal{A}_{T,L}\rangle|^2\right). \tag{2.34}$$

2.4 Energy dependence of parameters

In the standard formulation, the proton profile function $T_p(\vec{b})$ is characterized by fixed parameters B_p and B_{hs}, which represent half of the average squared radius of the proton and the hot spot, respectively. However, to account for energy-dependent effects and further enhance the model's accuracy, it is desirable to introduce an energy-dependent B_p and B_{hs}.

The energy-dependent $B_p(W)$, where W represents the energy of the system, is introduced based on measurements from HERA [34] that leads to the formula

$$B_p(W) = B_0 + 4\alpha' \ln\left(\frac{W}{W_0}\right), \tag{2.35}$$

which demonstrates that $B_p(W)$ follows a logarithmic scaling with respect to the W. Parameters B_0, W_0 and α' obtained from a fit to data are listed in Table 2.3.

$Q^2\,[\mathrm{GeV}^2]$	$B_0\,[\mathrm{GeV}^{-2}]$	$\alpha'\,[\mathrm{GeV}^{-2}]$	$W_0\,[\mathrm{GeV}]$
$\lesssim 1$	4.63	0.164	90
$2-80$	3.86	0.019	90

Table 2.3: The parameters corresponding to energy dependent radius of the proton with slope parameterization from [34].

Furthermore, we can also take into account the energy dependence of the B_{hs} using following formula

$$B_{hs}(x) = k\left(\frac{x}{x_0}\right)^{\lambda}, \tag{2.36}$$

where k is parameter, that will be shown in the following chapter. This expression shows that $B_{hs}(x)$ is inversely related to the saturation scale Q_s^2 defined in (2.18). Q_s^2 represents a scale on which we see the saturated region. If we increase the scale, we should see bigger details of hot spots, and what seemed to be one hot spot at a certain scale may be more smaller hot spots at bigger scale. Consequently, the number of hot spots, N_{hs}, needs to be compensated, which is achieved by modifying the parameters p_0, p_1, and p_2.

Combining the energy-dependent B_p and B_{hs} within the Hot-spot model provides a more comprehensive and realistic description of the proton structure and the distribution of hot spots.

	λ	x_0
GBW	0.287	$1.11 \cdot 10^{-4}$
Hot spot	0.21	$2 \cdot 10^{-4}$

Table 2.4: The table presents the parameters associated with the GBW [21] and Hot-spot [29] parameterizations.

	$B_p\,[\mathrm{GeV}^{-2}]$	$B_{hs}\,[\mathrm{GeV}^{-2}]$	p_0	p_1	p_2
A	4.7	0.8	0.011	-0.58	300
B	$B_0 + 4\alpha' \ln(W/W_0)$	0.8	0.01	-0.65	200
C	4.7	$1/2(x/x_0)^{\lambda}$	0.008	-0.69	200
D	$B_0 + 4\alpha' \ln(W/W_0)$	$1/2(x/x_0)^{\lambda}$	0.0085	-0.67	200

Table 2.5: The table provides an overview of the parameter values p_0, p_1 and p_2 corresponding to different scenarios *(A-D)* in the Hot-spot model.

Table 2.5 presents a summary of parameter values p_0, p_1, and p_2 corresponding to different scenarios labeled *(A-D)* within the Hot-spot model. In scenario A, both parameters B_p and B_{hs} are fixed. Scenario B features an energy-dependent $B_p(W)$ while keeping B_{hs} fixed. In scenario C, B_p remains fixed, but $B_{hs}(x)$ is energy-dependent.

Finally, scenario D considers both $B_p(W)$ and $B_{hs}(x)$ energy-dependent. For scenarios C and D, the parameter k was chosen as $1/2$.

The following figures provide visualizations of the transverse profile of the proton, illustrating its shape under different scenarios *(A-D)*.

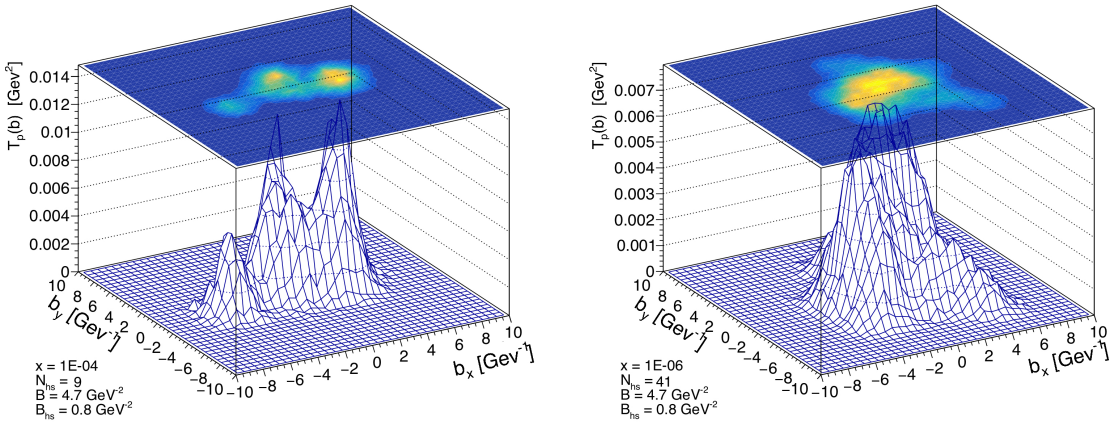

Figure 2.4: A) Shape of the transverse profile of the proton generated from Hot-spot model with fixed B_p and B_{hs} for different values of x.

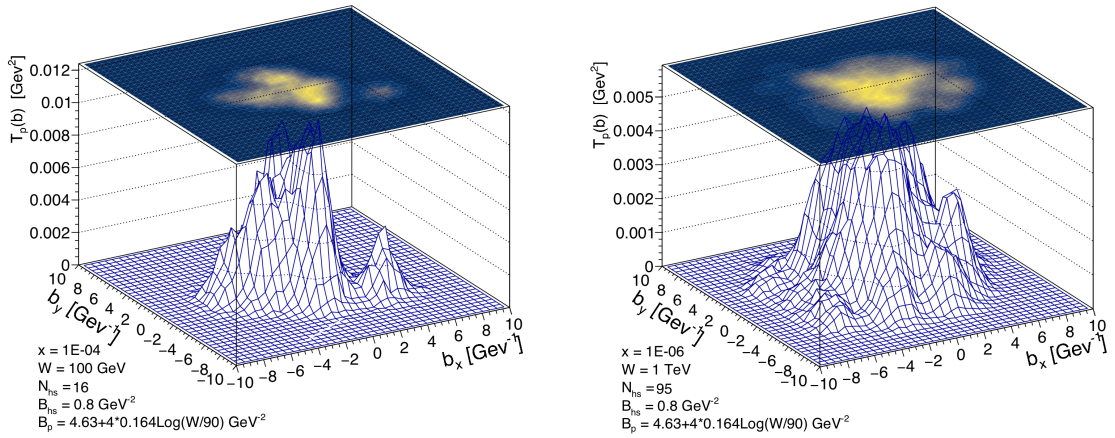

Figure 2.5: B) Shape of the transverse profile of the proton generated from Hot-spot model with energy dependent $B_p(W)$ and fixed value of B_{hs} for different values of x.

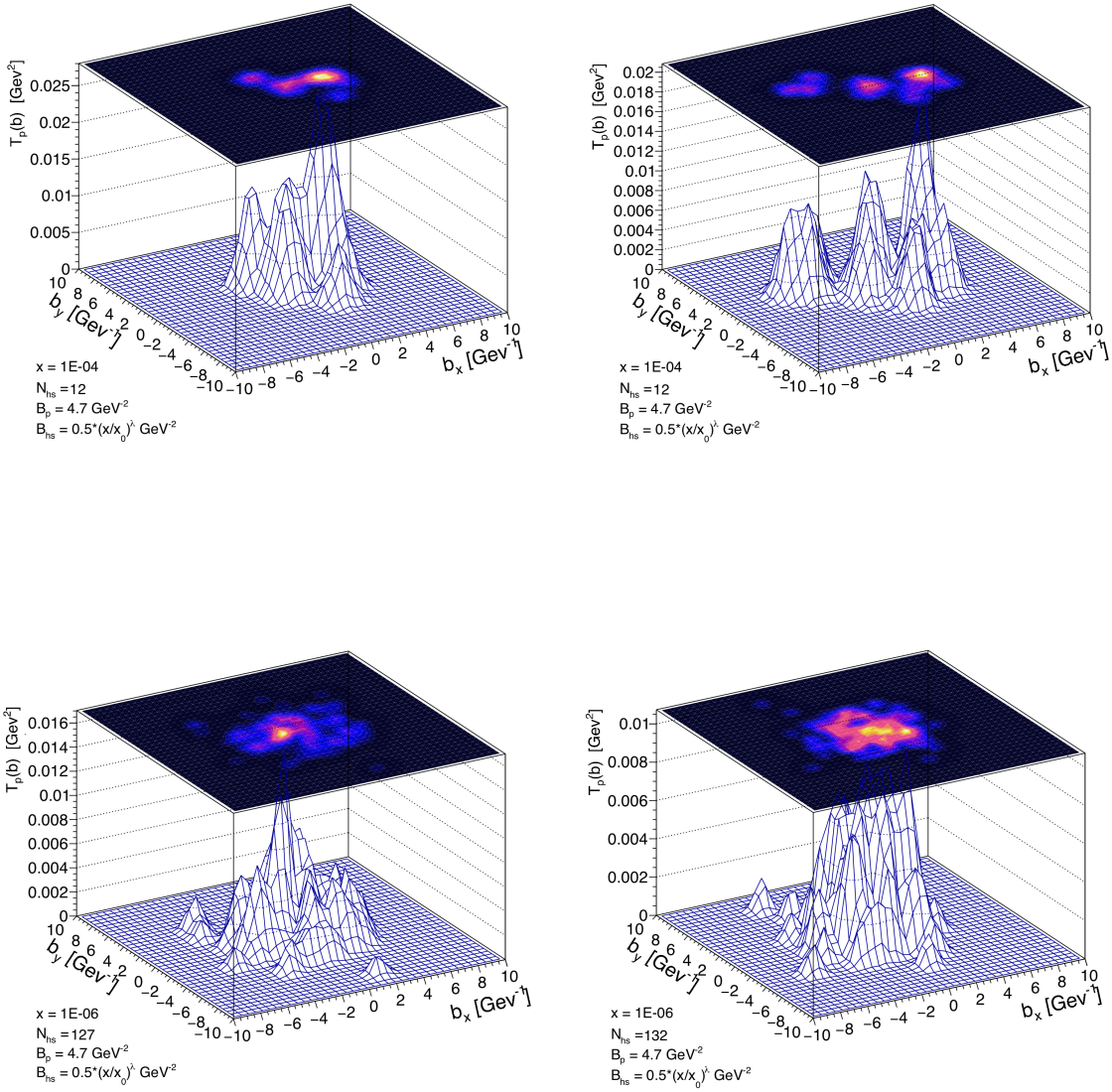

Figure 2.6: C) Shape of the transverse profile of the proton generated from Hot-spot model with fixed value of B_p and energy dependent $B_{hs}(x)$ for different values of x.

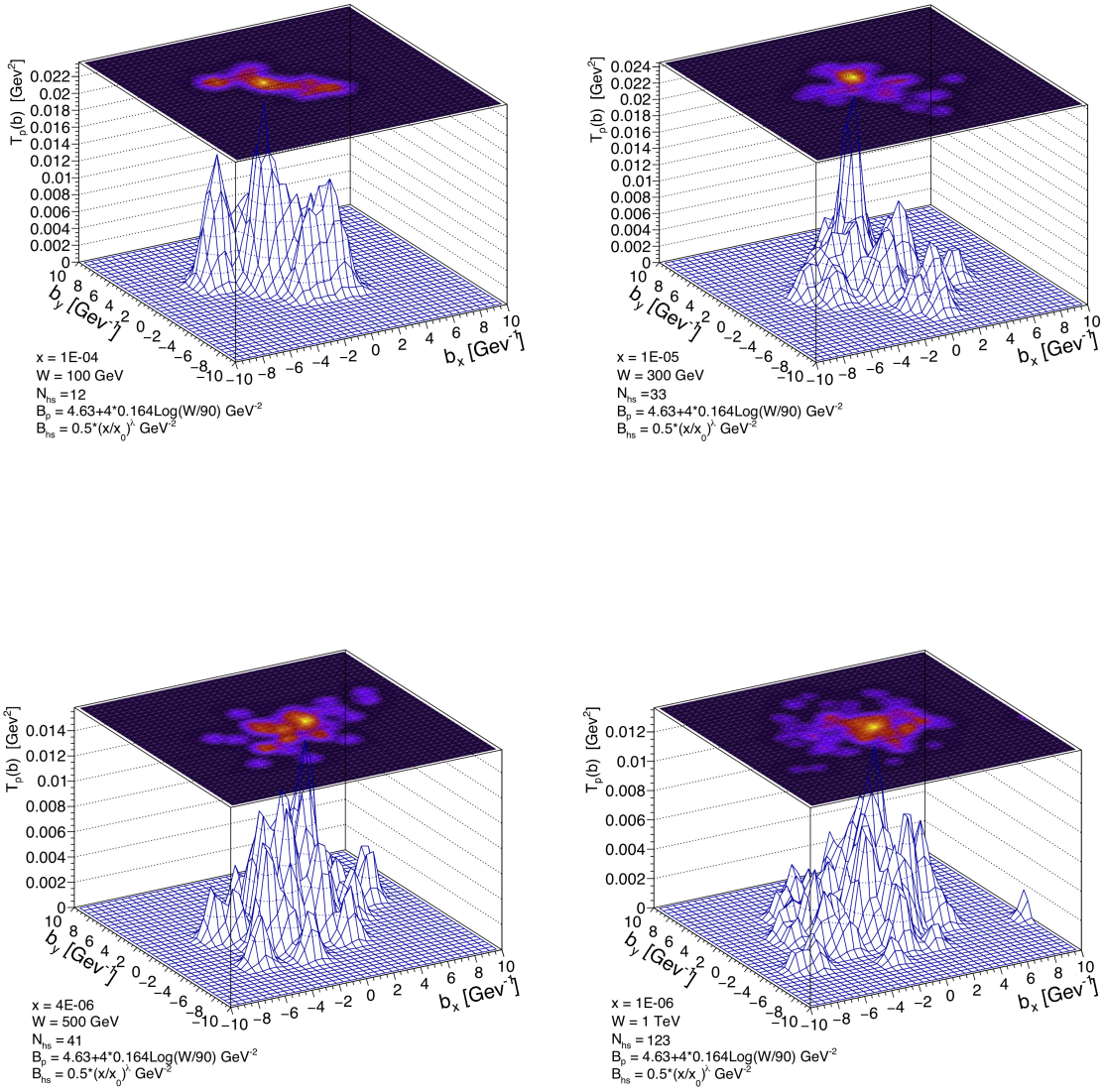

Figure 2.7: D) Shape of the transverse profile of the proton generated from Hot-spot model for energy dependent $B_p(W)$ and $B_{hs}(x)$ for different values of x.

Chapter 3

Results

My research is primarily focused on studying differential and total cross sections for exclusive and dissociative vector meson production. The initial part of the study introduces the cross section predictions obtained using the GBW parameterization in combination with Gaussian distribution for the proton's transverse profile function. Subsequent sections focus on predictions obtained with the Hot-spot model, as well as various modifications to this model. The results are then compared with the experimentally measured data.

3.1 Cross section with GBW model

In this section the predictions for the differential and total cross section for exclusive production of J/ψ, ρ and ϕ mesons are presented. These predictions are calculated using relations (2.9) and (2.10). The amplitude for exclusive vector meson production can be expressed as given in equation (2.23), where the integral over the dipole sizes, denoted by A_r, is governed by A_z and the dipole scattering amplitude $N(x, r)$. Here, the dipole scattering amplitude $N(x, r)$ is obtained using the GBW parameterization (2.18) with parameters specified in Table 2.4. The parameter σ_0 is determined through the relation $\sigma_0 = 4\pi B_p$, where B_p is chosen as $B_p = 4$ GeV^{-2} [31], except for the photoproduction of ρ meson, where B_p is set to 8 GeV^{-2} for normalization purposes [30]. The component A_b of the photon-proton scattering amplitude depends on the proton profile function function $T_p(b)$, which is in this case represented by the the Gaussian distribution (2.20). The integral over b is computed numerically using Simpson's rule [33]. Both the boosted Gaussian and Gaus-LC prescriptions for the wave functions are used. The predictions are compared to experimental data obtained from the H1 and ZEUS experiments at HERA [34–39].

Figure 3.1 displays the differential cross section as a function of momentum transfer $|t|$ for different values of Q^2, while keeping W fixed at 75 GeV^2 for the ρ and ϕ mesons, and $W = 100$ GeV^2 for the J/ψ meson. Figure 3.2 shows the comparison of the predictions to the data for the total cross section of exclusive vector meson production. The model exhibits good agreement with the data, particularly at low values of Q^2.

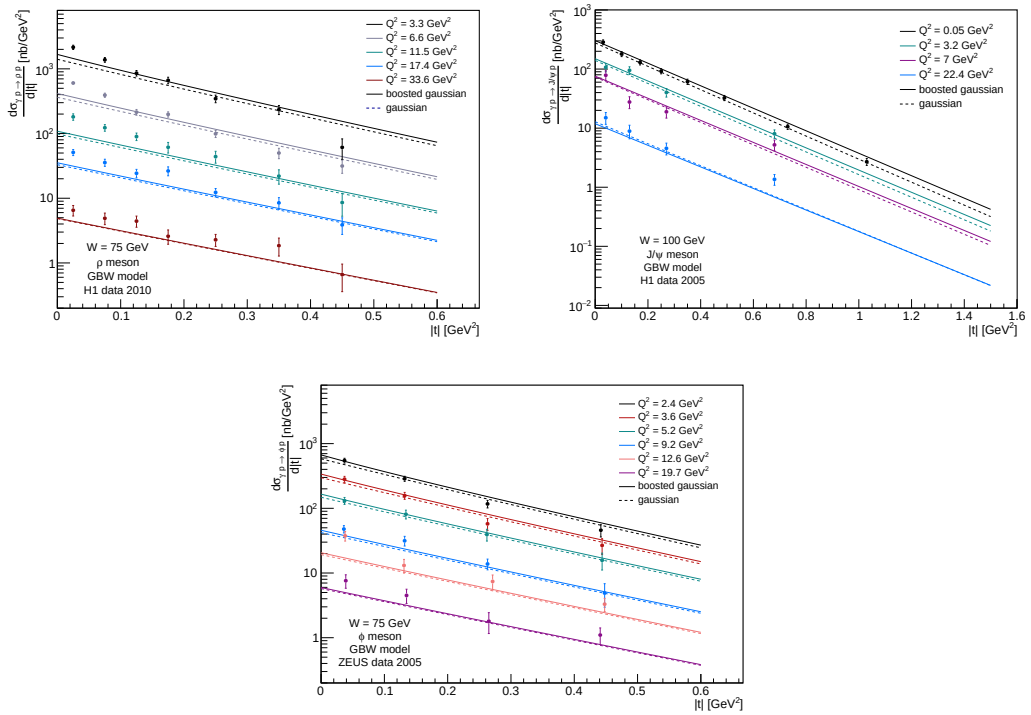

Figure 3.1: Differential cross section for exclusive production of J/ψ, ρ and ϕ mesons using GBW parameterization. Predictions are compared to the data [36], [34], [35].

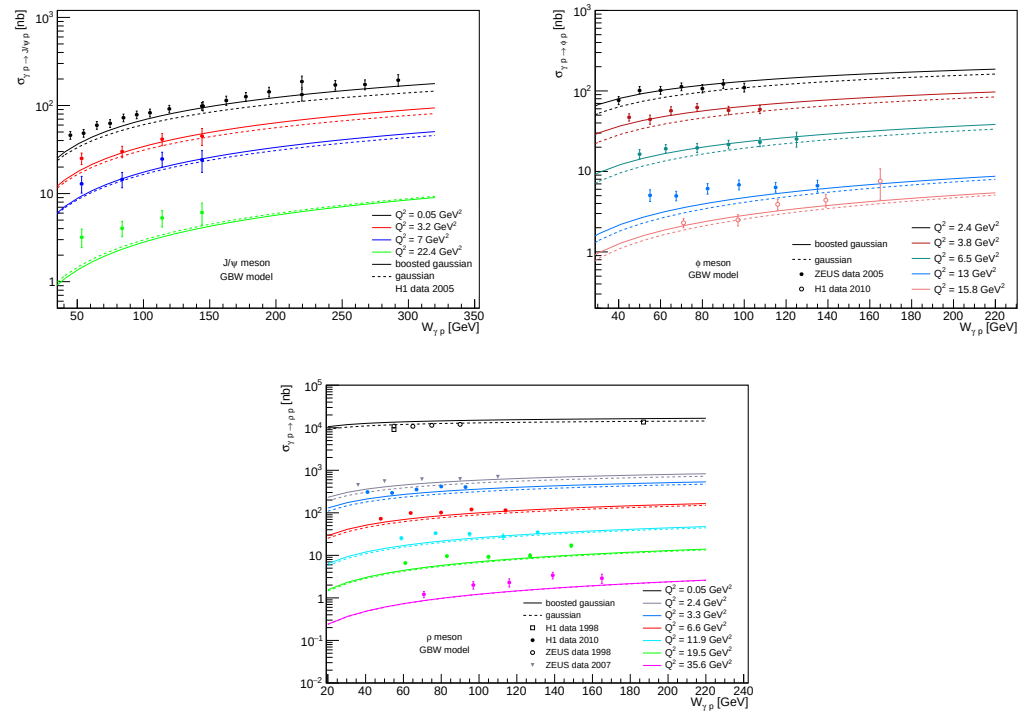

Figure 3.2: Total cross section of exclusive production of J/ψ, ρ and ϕ mesons using GBW parameterization. Predictions are compared to the data [36], [34], [35], [37], [38] [39].

3.2 Hot-spot model

Applying the formalism of the Hot-spot model, as described in section 2.3, the cross sections for the exclusive and dissociative production of a vector mesons are calculated. This computation is performed using 10000 configurations of the proton profile function for each value of x. The dipole scattering amplitude is obtained from the GBW parameterization (2.18) with the parameter values given in Table 2.4. The parameter σ_0 is formulated as $\sigma_0 = 4\pi B_p$ and B_p is fixed at 4.7 GeV^{-2}. In order to describe the normalization of the photoproduction of the ρ meson, the value of B_p is set to $B_p = 8$ GeV^{-2} [30]. Additionally, the average of the squared transverse radius of a hot spot is assigned as $B_{hs} = 0.8$ GeV^{-2}, and parameter values for the energy dependent number of hot spots $N_{hs}(x)$ (2.29) can be found in Table 2.5.

Differential cross section with Hot-spot model

Figure 3.3 displays the differential cross section for the exclusive production of a vector meson with respect to $|t|$. The model predictions align well with experimental data for the ϕ and ρ mesons. However, when comparing the predictions for the J/ψ meson, it becomes apparent that the predicted curve follows the correct slope mainly at low $|t|$.

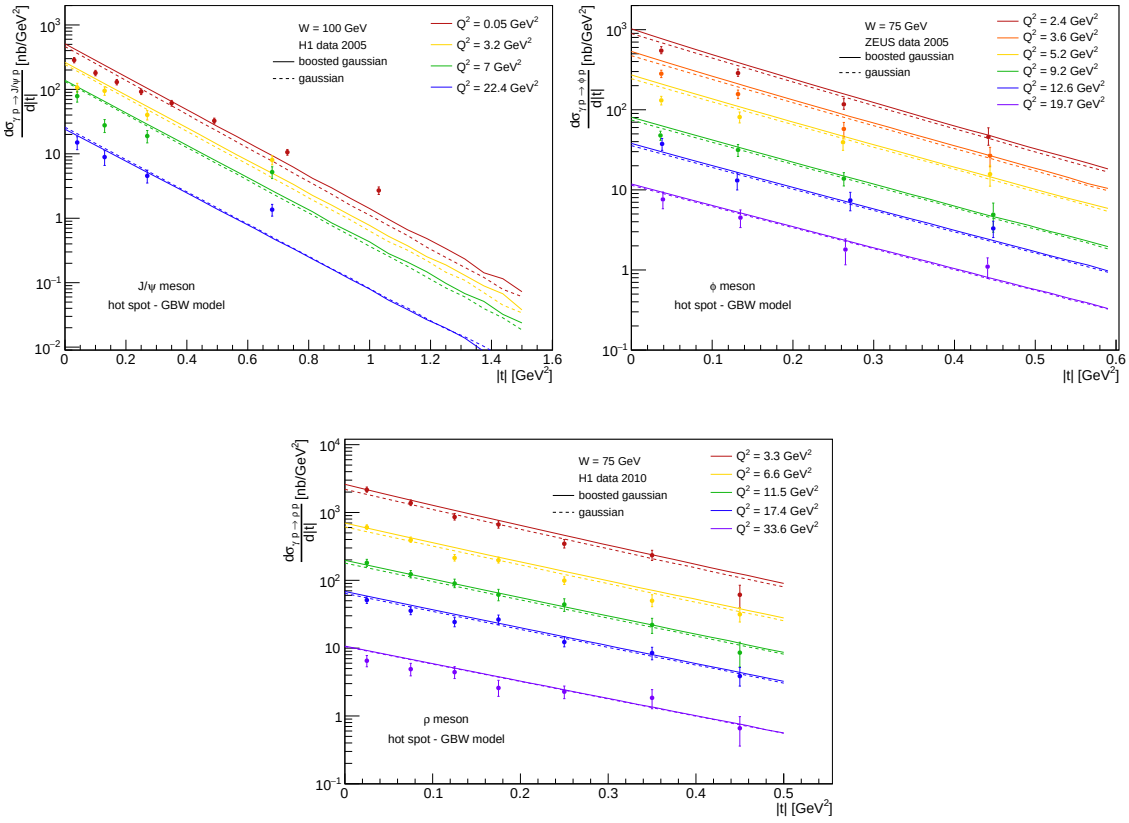

Figure 3.3: Differential cross section for exclusive production of J/ψ, ρ and ϕ mesons using Hot-spot model with GBW parameterization. Predictions are compared to the data [35], [34], [36].

Figures 3.4 and 3.5 present the W dependence of the exclusive and dissociative differential cross sections for J/ψ meson photoproduction and electroproduction at fixed values of $|t|$. The model predictions for exclusive production are compared to experimental data [34]. Overall, the results show a reasonable level of agreement for exclusive photoproduction, however, for higher values of $|t|$, the model tends to underestimate the data. For electroproduction, the closest agreement with the data occurs at $|t| = 0.19$ GeV^2. For the dissociative differential cross sections for J/ψ production at fixed values of $|t|$ no data are available for comparison.

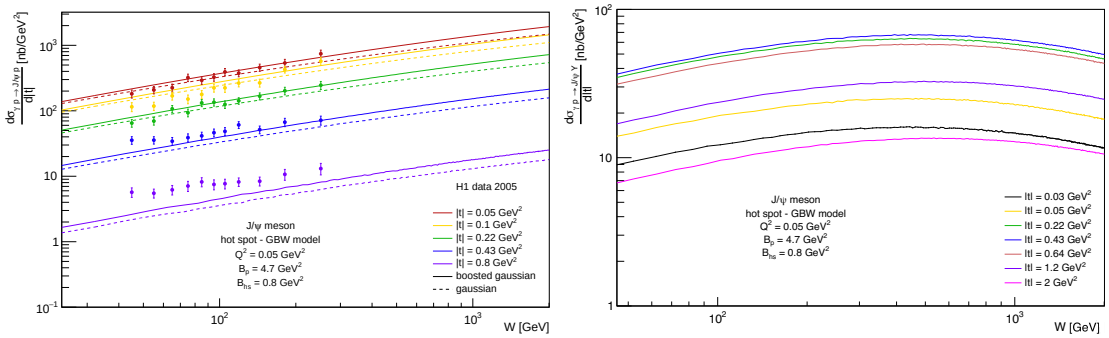

Figure 3.4: The W dependence of differential cross section at fixed value of $|t|$ for exclusive (left) and dissociative (right) J/ψ photoproduction.

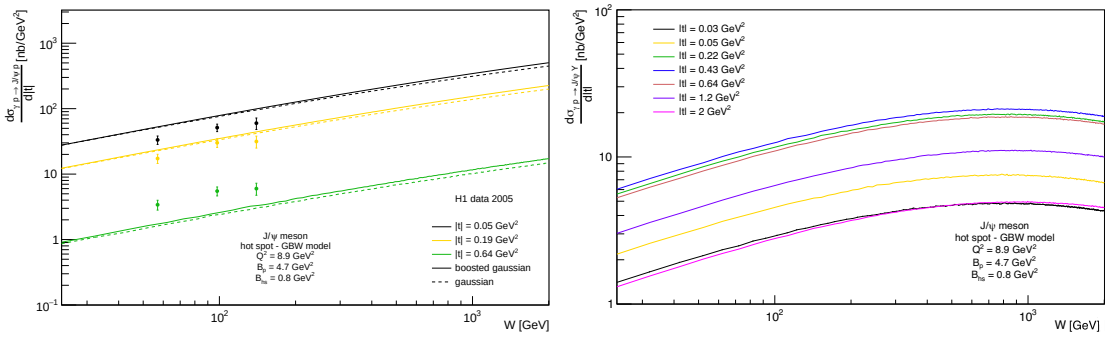

Figure 3.5: The W dependence of differential cross section at fixed value of $|t|$ for exclusive (left) and dissociative (right) J/ψ electroproduction.

Total cross section with Hot-spot model

Figures 3.6 to 3.9 show the predictions for the total cross section of exclusive and dissociative production of the ϕ, ρ, J/ψ, and $\Upsilon(1S)$ vector mesons as functions of W, for several values of Q^2. Our predictions are compared with measurements from various experiments, including H1 [34,36,37,40,41], ZEUS [35,38,39,42], ALICE [45,46], CMS [44], and LHCb [43]. The model's predictions for the exclusive cross sections of the ϕ, ρ, and J/ψ align well with the experimental data. However, due to the uncertainty in the $\Upsilon(1S)$ exclusive photoproduction measurements, definitive conclusions cannot be made at this time.

In the case of dissociative production, the model yields satisfactory results for the ϕ meson at high values of W, at lower values of W, the trend tends to overestimate the data. For the ρ meson, the model results for $Q^2 = 3.3$ GeV^2 and $Q^2 = 7.5$ GeV^2 are in agreement with the data; however, for higher virtualities, the data are overestimated. Regarding the dissociative production of the J/ψ meson, the predictions align well with the data when using the boosted Gaussian parameterization. The data for the dissociative production of the $\Upsilon(1S)$ meson are are currently unavailable.

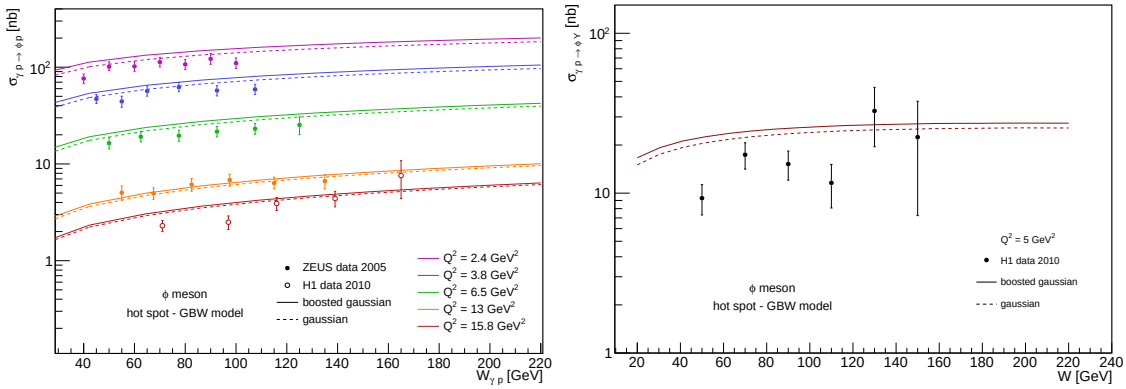

Figure 3.6: Comparison of the model predictions for the total cross section of exclusive (left) and dissociative (right) ϕ production with H1 [36] and ZEUS [35] data.

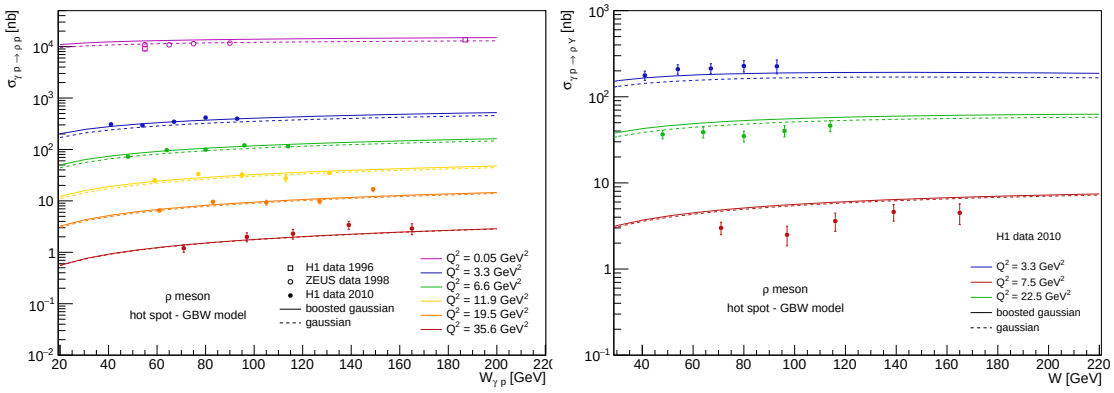

Figure 3.7: Comparison of the model predictions for the total cross section of exclusive (left) and dissociative (right) ρ production with H1 [36], [37] and ZEUS [38] [39] data.

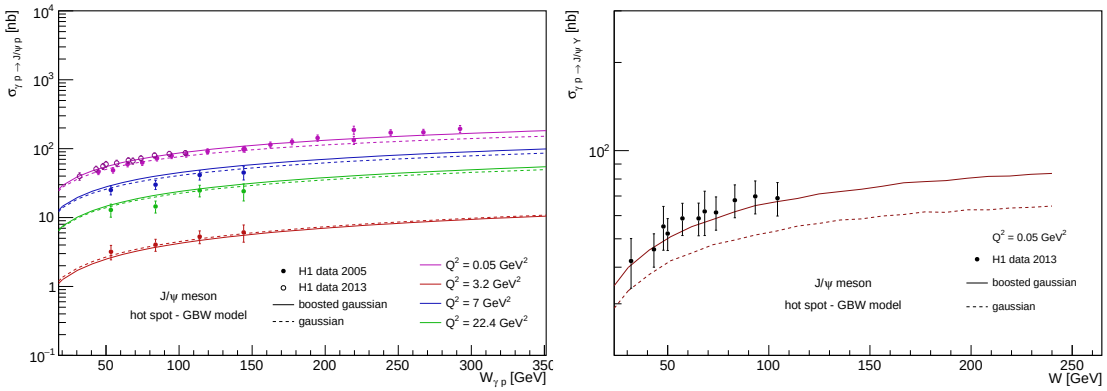

Figure 3.8: Comparison of the model predictions for the total cross section of exclusive (left) and dissociative (right) J/ψ production with H1 [34], [40] data.

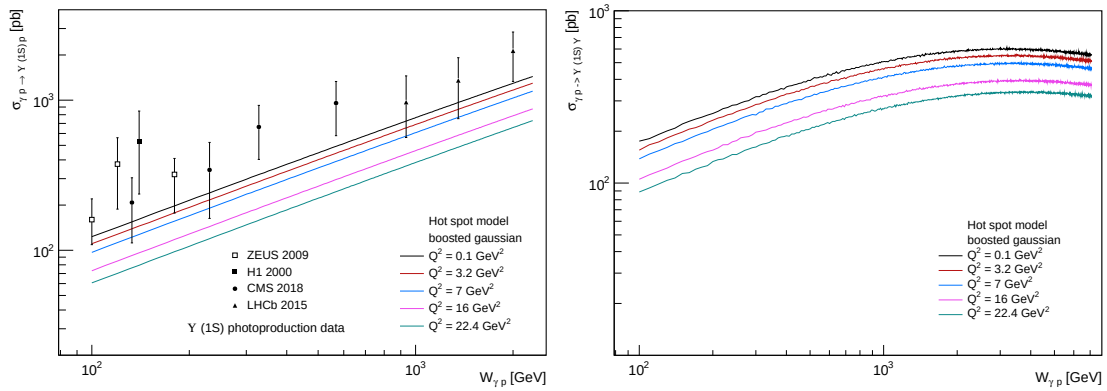

Figure 3.9: Comparison of the model predictions for the total cross section of exclusive (left) $\Upsilon(1S)$ production with H1 [41], ZEUS [42], CMS [44] and LHCb [43] data and model predictions for the W dependence of the dissociative (right) production cross section of a $\Upsilon(1S)$ vector meson.

3.3 Energy dependent B_p and B_{hs}

Up to this point, we were assuming that B_p and B_{hs} are fixed parameters, determined by fitting the HERA data [29, 34, 40]. This straightforward approach describes the experimental data rather well. In Figures 3.10 and 3.11 we present a comparison of the total cross section of J/ψ production with the H1 data [34, 40] using various choices of parameters B_p and B_{hs}. Only the boosted Gaussian wave function parameterization is used.

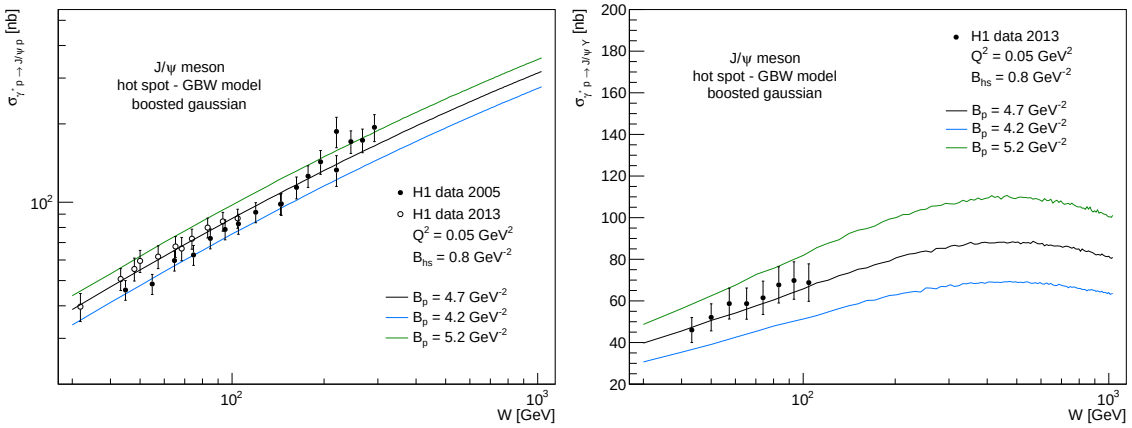

Figure 3.10: Comparison of various options of the B_p parameter for total cross section of exclusive (left) and dissociative (right) J/ψ photoproduction.

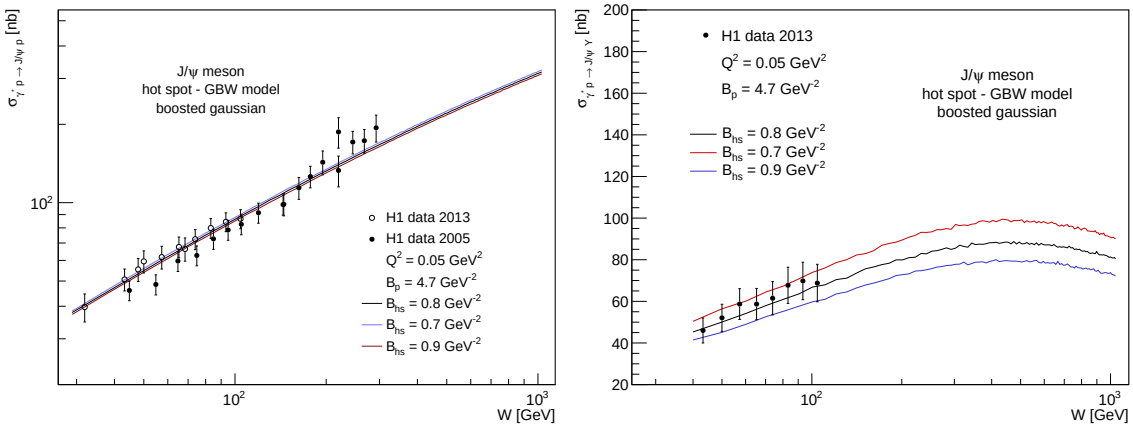

Figure 3.11: Comparison of various options of the B_{hs} parameter for total cross section of exclusive (left) and dissociative (right) J/ψ photoproduction.

Energy dependent slope parameter

In Figures 3.12 and 3.13 we present a comparison between the fixed value of parameter $B_p = 4.7$ GeV^{-2} and the energy-dependent $B_p(W)$, defined as (2.35). The exclusive photoproduction cross section is compared with the H1 data from HERA [34, 40] and the ALICE p-Pb data [45, 46].

The energy-dependent $B_p(W)$ follows a logarithmic scaling with respect to W, indicating the growth of the proton size with energy. As a result, the number of hot spots requires adjustments. When the proton is larger, more hot spots is needed to fill the phase space. To achieve this, we modify the parameters p_0, p_1, and p_2. Their values are listed in Table 2.5 scenario B. The change in the number of hot spots, along with the ratio of the exclusive and dissociative cross section, can be seen in Figure 3.14. Both approaches provide a good description of the data for exclusive J/ψ photoproduction; nevertheless, the model with energy-dependent $B_p(W)$ aligns more closely with the ALICE data at low W, while the H1 data at low W are better described when B_p is kept fixed. However, for high values of W, the model with energy-dependent $B_p(W)$ tends to overestimate the ALICE data. Both approaches provide good descriptions of the data for dissociative vector meson production.

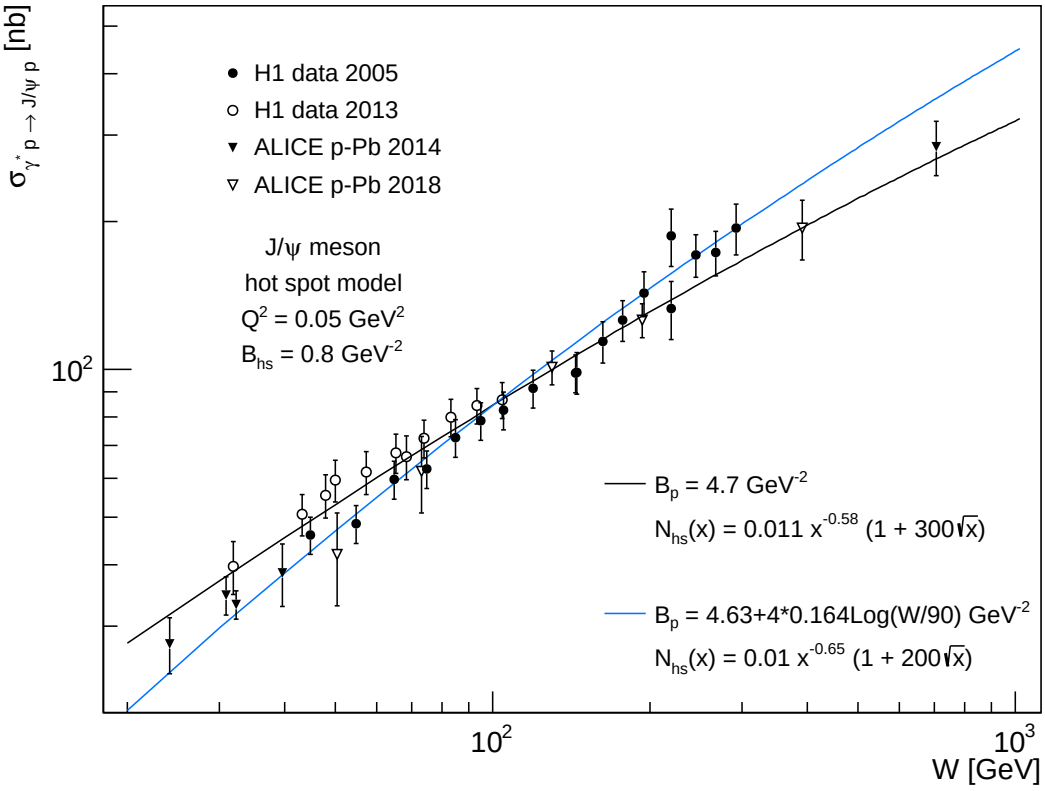

Figure 3.12: Comparison of the model predictions for the total cross section of exclusive J/ψ photoproduction using fixed B_p (black line) and energy-dependent $B_p(W)$ (blue line) with H1 [34], [40] and ALICE [45], [46] data.

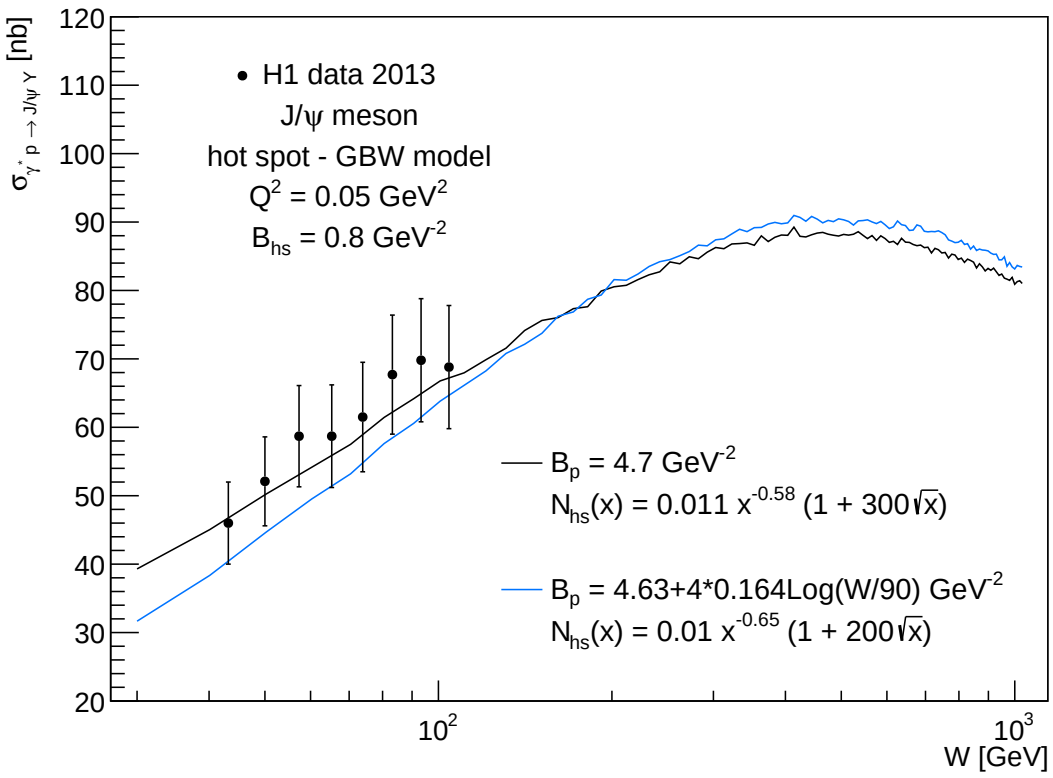

Figure 3.13: Comparison of the model predictions for the total cross section of dissociative J/ψ photoproduction using fixed B_p (black line) and energy-dependent $B_p(W)$ (blue line) with H1 [34], [40] data.

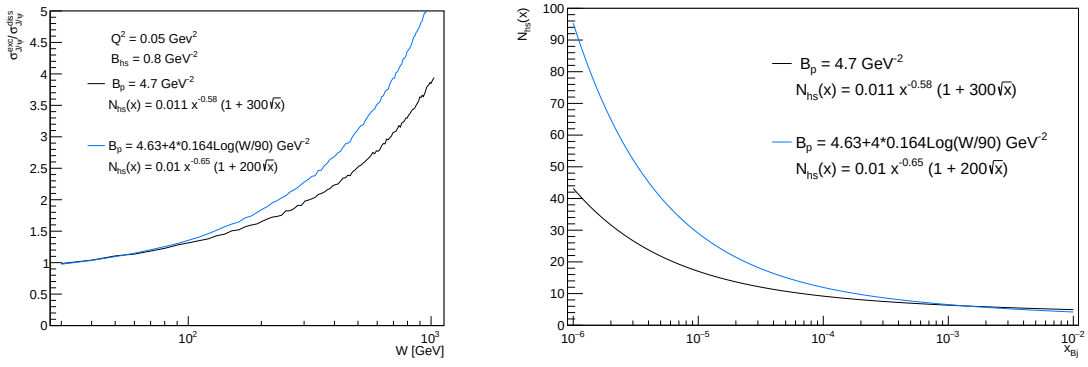

Figure 3.14: Ratio of the exclusive and dissociative cross section (left). Number of hot spots $N_{hs}(x)$ as a function of x for energy-dependent and energy-independent slope parameter (right).

Energy dependent hot spot radius

Next, we maintain a fixed value for B_p at $B_p = 4.7$ GeV^{-2} and consider $B_{hs}(x)$ to be inversely related to the saturation scale, as described by equation (2.36), and discussed in the previous chapter. As we apply this prescription for hot spot radius, at higher energies, smaller hot spots will emerge, necessitating a corresponding adjustment in N_{hs}, see Table 2.5 scenario C. The parameter k from (2.36) is set to 1/2.

The model with an energy-dependent hot spot radius, $B_{hs}(x)$, shows good correspondence with the data for the total cross section of both exclusive (Figure 3.15) and dissociative (Figure 3.16) J/ψ photoproduction.

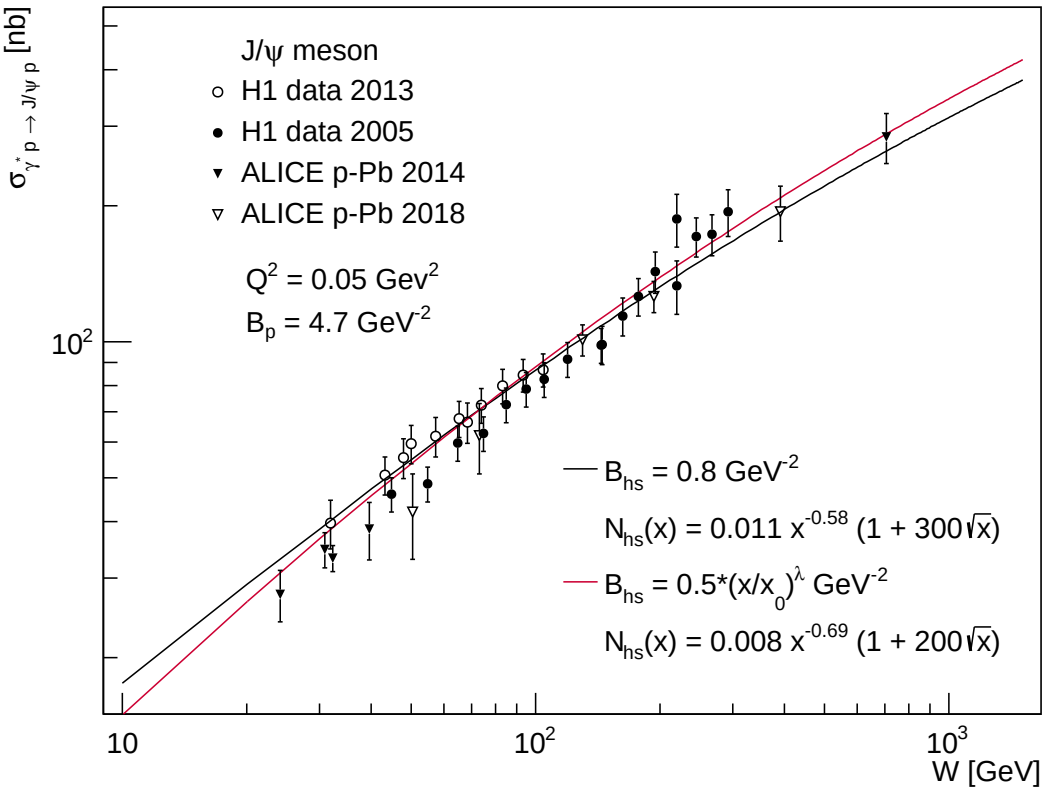

Figure 3.15: Comparison of the model predictions for the total cross section of exclusive J/ψ photoproduction using fixed B_{hs} (black line) and energy-dependent $B_{hs}(x)$ (red line) with H1 [34], [40] and ALICE [45], [46] data.

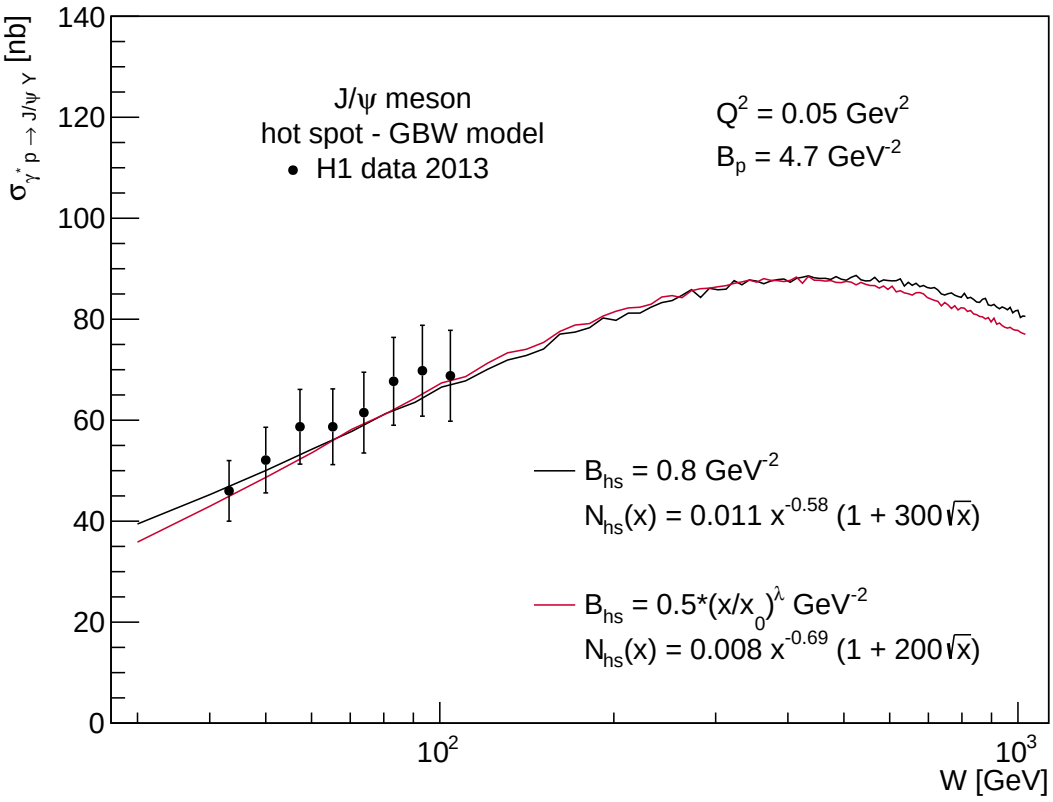

Figure 3.16: Comparison of the model predictions for the total cross section of dissociative J/ψ photoproduction using fixed B_{hs} (black line) and energy-dependent $B_{hs}(x)$ (red line) with H1 [34], [40] data.

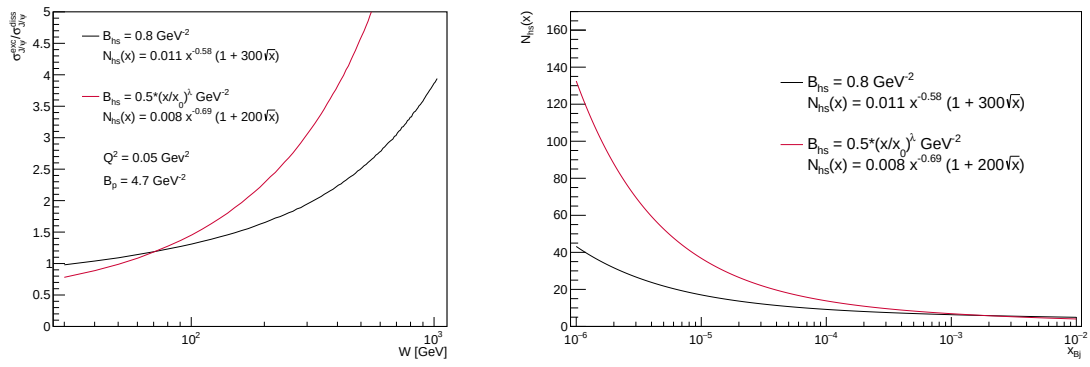

Figure 3.17: Ratio of the exclusive and dissociative cross section (left). Number of hot spots $N_{hs}(x)$ as a function of x for energy-dependent and energy-independent hot spot radius (right).

Energy dependent proton and hot spot radius

Our goal is to incorporate the energy dependence of both B_p and B_{hs} into the Hot-spot model to provide a more realistic description of the proton structure.

Figures 3.18 and 3.19 show the total cross section for exclusive and dissociative photoproduction of J/ψ meson. The model with energy dependent parameters shows good agreement with the data for exclusive photoproduction, particularly for low values of W, around 30 GeV, whereas the model with fixed B_p and B_{hs} overestimates the data in this region.

Figure 3.21 displays the W dependence of the exclusive and dissociative differential cross sections for J/ψ meson photoproduction and electroproduction at fixed values of $|t|$. Solid line represents the model with energy dependent $B_p(W)$ and $B_{hs}(x)$, while the dash-dotted line represents the model with fixed B_p and B_{hs}.

Figure 3.22 illustrates the W dependence of the exclusive and dissociative total cross sections for ϕ meson for various values of Q^2. Similarly, Figure 3.23 presents the the W dependence for the total cross sections of the ρ meson. Due to the normalisation, the B_p for ρ meson photoproduction is set to 8 GeV^{-2} and energy dependent $B_p(W)$ is given by $B_p(W) = 8 + 4 \cdot 0.164 \ln W/90$ GeV^{-2}.

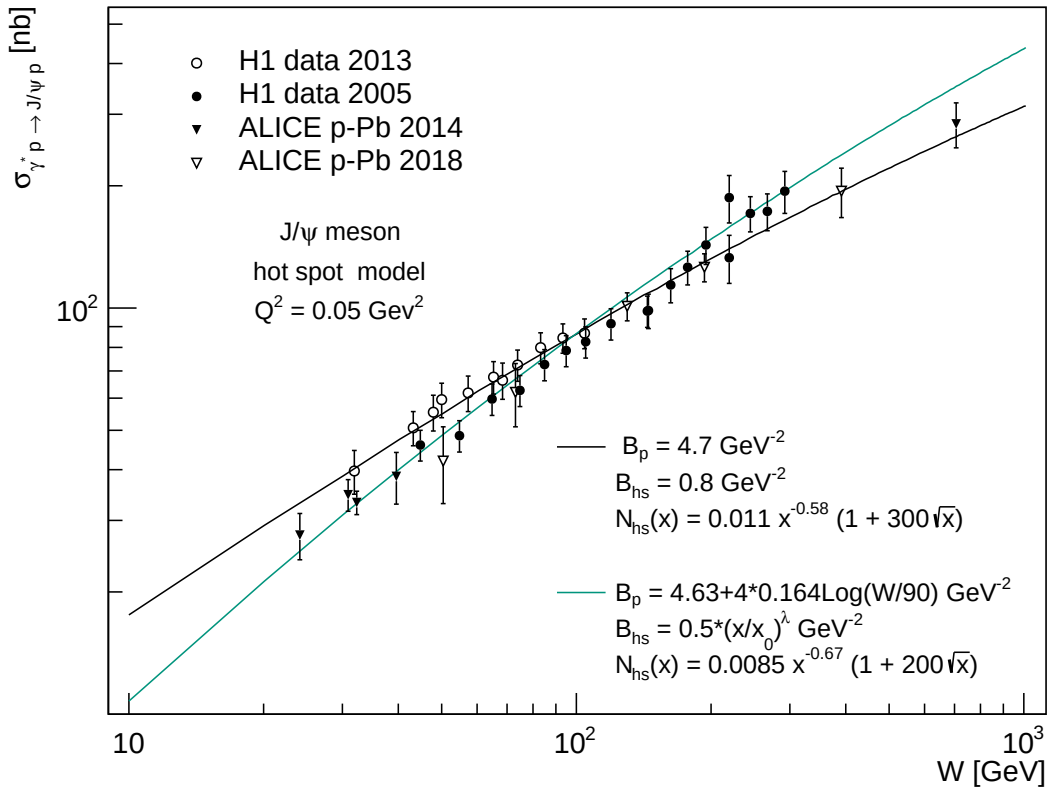

Figure 3.18: Comparison of the model predictions for the total cross section of exclusive J/ψ photoproduction using fixed B_p and B_{hs} (black line) and energy dependent $B_p(W)$ and $B_{hs}(x)$ (green line) with H1 [34], [40] and ALICE [45], [46] data. Values of $N_{hs}(x)$ parameters are: $p_0 = 0.0085$, $p_1 = -0.67$ and $p_2 = 200$.

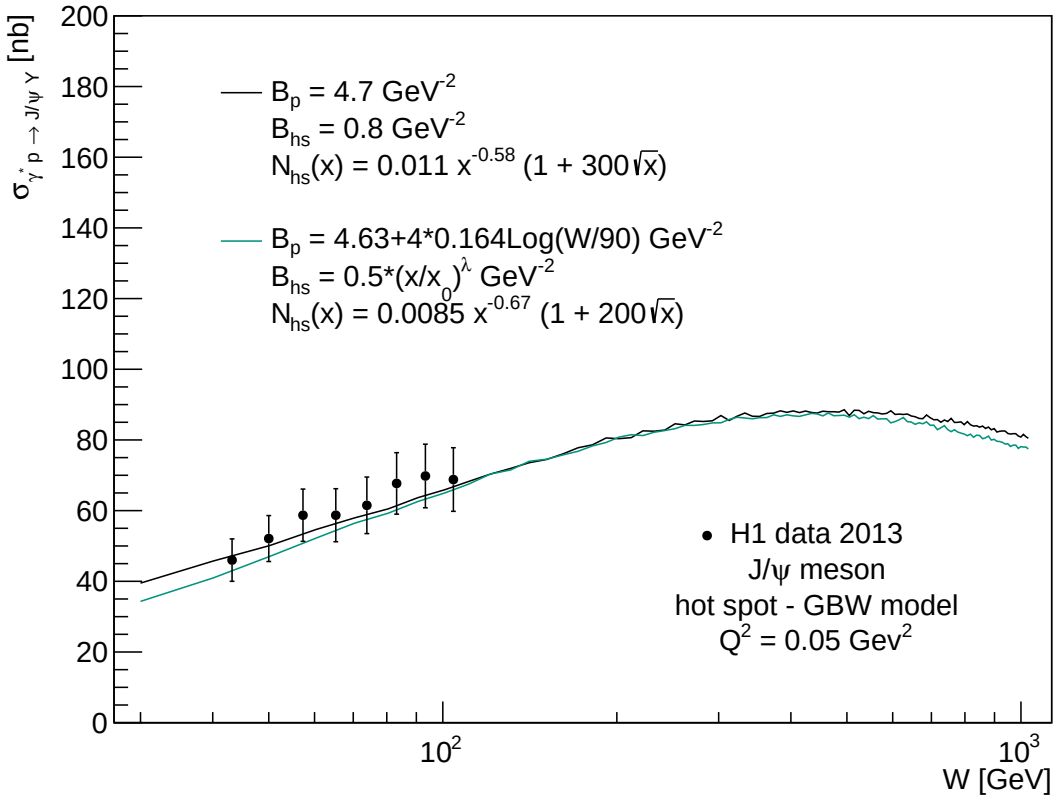

Figure 3.19: Comparison of the model predictions for the total cross section of dissociative J/ψ photoproduction using fixed B_p and B_{hs} (black line) and energy dependent $B_p(W)$ and $B_{hs}(x)$ (green line) with H1 [34], [40] data. Values of $N_{hs}(x)$ parameters are: $p_0 = 0.0085$, $p_1 = -0.67$ and $p_2 = 200$.

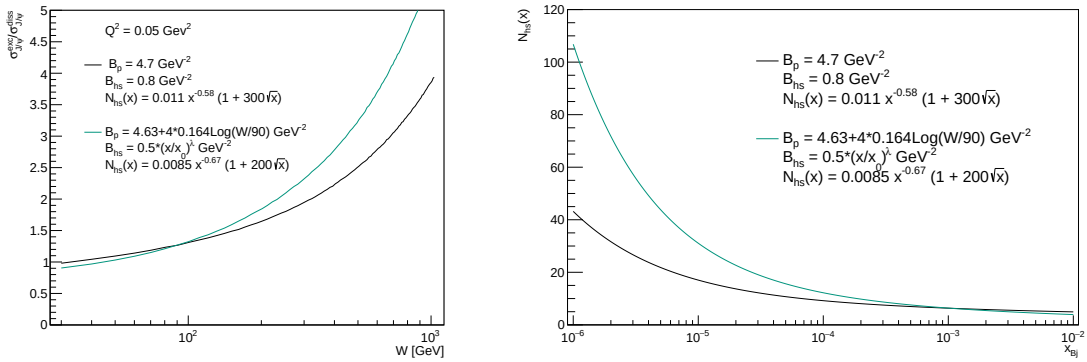

Figure 3.20: Ratio of the exclusive and dissociative cross section (left). Number of hot spots $N_{hs}(x)$ as a function of x for energy dependent and energy independent B_p and B_{hs} (right).

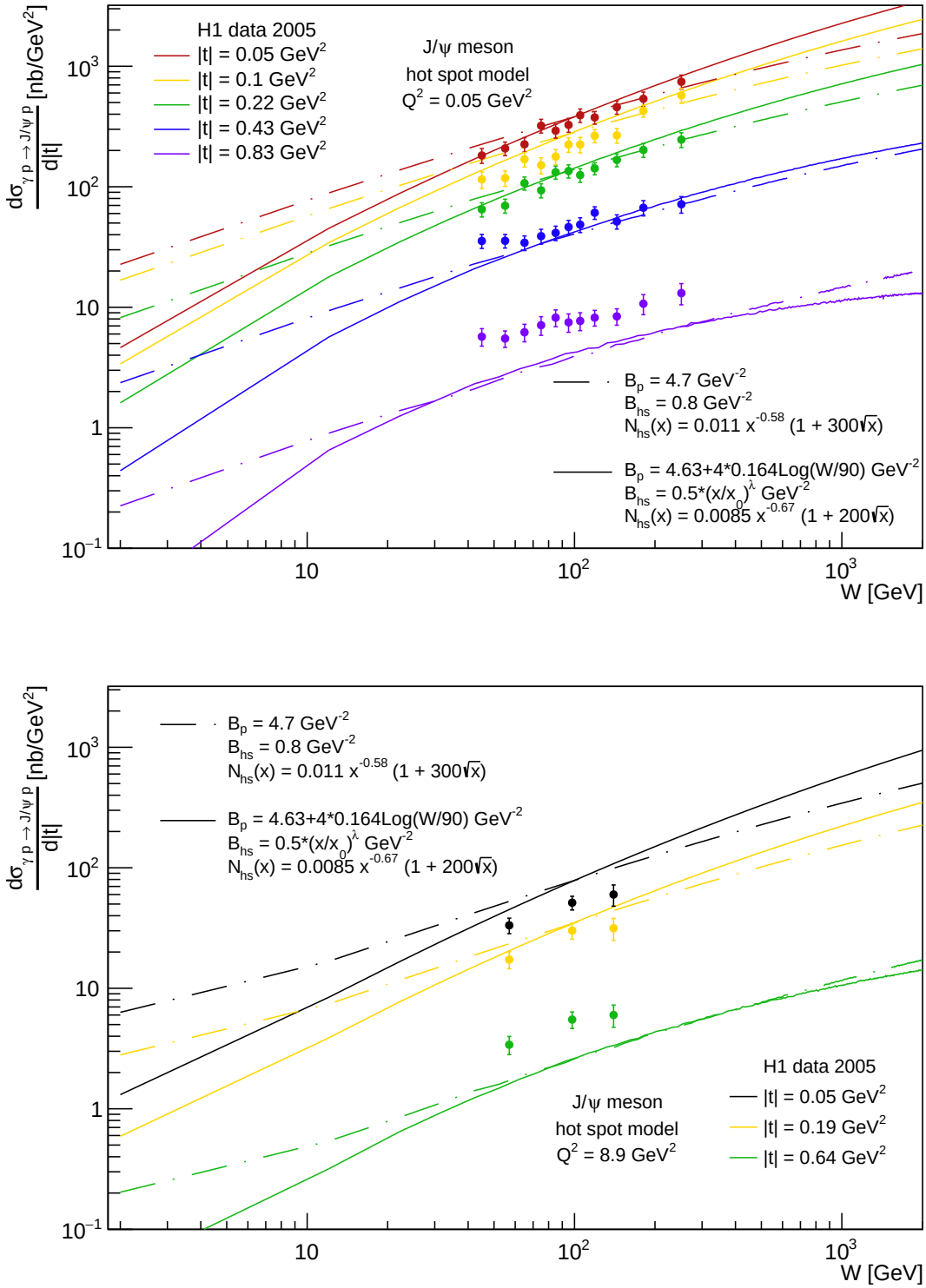

Figure 3.21: The W dependence of differential cross section at fixed values of $|t|$ for exclusive J/ψ photoproduction (upper plot) and electroduction (lower plot).

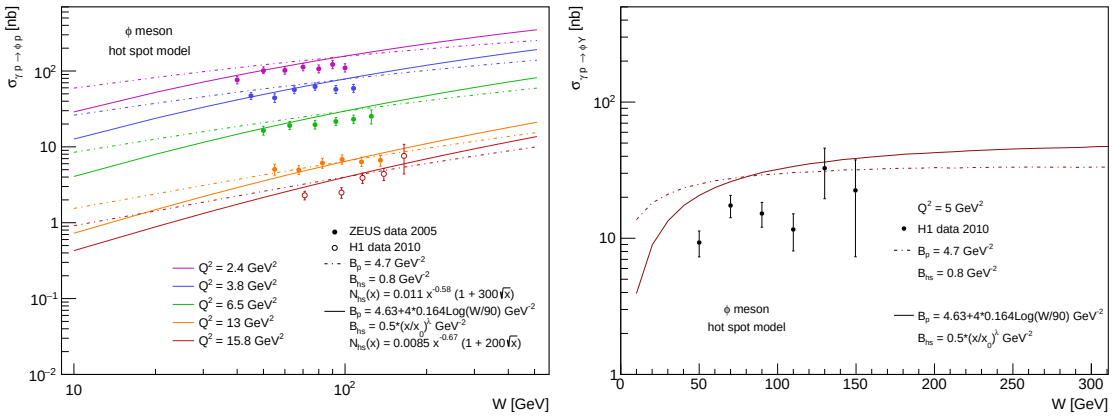

Figure 3.22: Comparison of the model predictions for the total cross section of exclusive (left) and dissociative (right) ϕ production using fixed B_p and B_{hs} (dash-dotted line) and energy dependent $B_p(W)$ and $B_{hs}(x)$ (solid line) with H1 [36] and ZEUS [35] data. Values of $N_{hs}(x)$ parameters are: $p_0 = 0.0085$, $p_1 = -0.67$ and $p_2 = 200$.

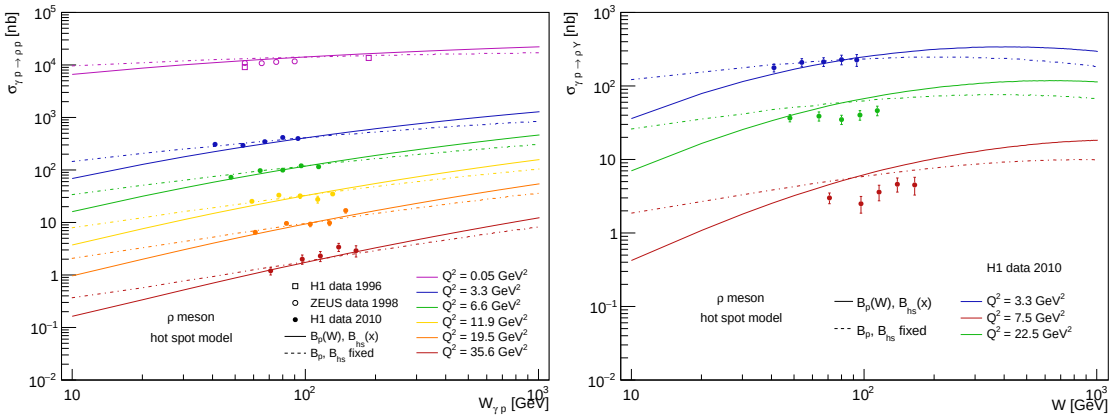

Figure 3.23: Comparison of the model predictions for the total cross section of exclusive (left) and dissociative (right) ρ production using fixed B_p and B_{hs} (dash-dotted line) and energy dependent $B_p(W)$ and $B_{hs}(x)$ (solid line) with H1 [36], [37] and ZEUS [38] [39] data. In the case of electroproduction is $B_p = 4.63 + 4 \cdot 0.164 \ln \frac{W}{90}$ GeV^{-2}, while for photoproduction is $B_p = 8 + 4 \cdot 0.164 \ln \frac{W}{90}$ GeV^{-2} due to the normalisation. Values of $N_{hs}(x)$ parameters are: $p_0 = 0.0085$, $p_1 = -0.67$ and $p_2 = 200$.

Conclusion

In this work, we explored the world of high-energy collisions to understand the proton's structure and the dynamics of vector meson production. Understanding the $\gamma^* p \to VMp$ process requires careful examination of the individual components of the scattering amplitude $\mathcal{A}_{T,L}^{\gamma^* p \to VMp}$ and the models used to describe them. The photon wave function can be obtained from Quantum Electrodynamics, as its properties are well understood. On the other hand, the vector meson wave function necessitates modeling to calculate its overlap with the virtual photon wave function. In our research, we utilized the Gaus-LC and boosted Gaussian model for this purpose. Another nontrivial component is the dipole-proton cross section. In this work, we employed a factorized form for the dipole amplitude, with $N(x, r)$ representing the $b-$independent dipole scattering amplitude based on the Golec-Biernat and Wusthoff model. The $b-$dependence of the dipole-proton cross section was then introduced by the the proton profile function function $T_p(b)$. Our focus was divided between two main approaches: the Gaussian distribution to describe the transverse profile, and the Hot-spot model, which considers the proton's structure as fluctuating hot spots, the number of which grows with decreasing x. The GBW parameterization in combination with Gaussian distribution provided good results when compared to the exclusive production data, which demonstrates the effectiveness of this simple and straightforward approach.

With the Hot-spot model, we studied four different scenarios based on the energy dependence of the size of the proton and sizes of hot spots. Having fixed $B_p = 4.7$ GeV^{-2} and $B_{hs} = 0.8$ GeV^{-2}, exept for the photoproduction of ρ meson, where $B_p = 8$ GeV^{-2}, the Hot-spot model shows generally good agreement with the data. However, for the differential cross section of exclusive J/ψ production, the predicted curve follow the correct slope mainly at low $|t|$. The comparison of the model predictions with the measured W dependence of the exclusive differential J/ψ photoproduction shows a good agreement at low values of $|t|$, however, at higher $|t|$, the model tents to underestimate the data. For the total cross section of the exclusive and dissociative production of ϕ, ρ and J/ψ the predictions are mostly consistent with the data. Also, the exclusive and dissociative cross section of the $\Upsilon(1S)$ meson was calculated, nevertheless due to the large uncertainties, no definitive conclusions can be drawn.

We further modified the Hot-spot model by introducing energy dependence in different components, seeking a more accurate representation of proton behavior at different energy levels. We explored the effects of introducing energy dependence in the proton size by parameterizing the proton's width as a function of W. The radius of the proton has a logarithmic growth with energy based on measurements from HERA [34]. We also considered the width of the hot spots to be inversly related to the saturation scale Q_s^2.

With increasing saturation scale, one should see partonic substructure more deatailed, as a consequence of the DGLAP evolution. We incorporated this phenomenon into our model, since this prescription implies a shrinking size of hot spots as the saturation scale increases. Additionally, we made both B_p and B_{hs} energy dependent. In all of these scenarios, there is a correlation between energy dependent parameter and the number of hot spots. We have shown that these approaches provide similarly good agreement with the data for the total cross section of exclusive and dissociative J/ψ production. These models generally demonstrate a steeper evolution of the total cross section of exclusive J/ψ, ϕ and ρ production compared to models with fixed B_p and B_{hs}.

Bibliography

[1] C.G. Callan, D.J. Gross *High-energy electroproduction and the constitution of the electric current*. Phys. Rev. Lett., vol. 22 (1969).

[2] R.P. Feynman *Very High-Energy Collisions of Hadrons*. Phys. Rev. Lett. 23 (1969) 1415.

[3] M. Thomson *Modern Particle Physics*. Cambridge University Press, New York (2013), ISBN: 9781107034266

[4] H1, ZEUS Collaborations, H. Abramowicz et al. *Combination of Measurements of Inclusive Deep Inelastic e±p Scattering Cross Sections and QCD Analysis of HERA Data*. Eur.Phys.J.C, vol. 75, no. 12 (2015).

[5] F. Halzen, A.D. Martin *QUARKS AND LEPTONS: AN INTRODUCTORY COURSE IN MODERN PARTICLE PHYSICS*. ISBN: 9780471887416 (1984).

[6] V.N. Gribov, L.N. Lipatov *Deep inelastic e p scattering in perturbation theory*. Sov. J. Nucl. Phys. 15, 438-450 (1972).

[7] V.N. Gribov, L.N. Lipatov *e+ e- pair annihilation and deep inelastic e p scattering in perturbation theory*. Sov. J. Nucl. Phys. 15, 675-684 (1972).

[8] Y.L. Dokshitzer *Calculation of the Structure Functions for Deep Inelastic Scattering and e+ e- Annihilation by Perturbation Theory in Quantum Chromodynamics.*. Sov. Phys. JETP 46, 641-653 (1977).

[9] G. Altarelli, G. Parisi *Asymptotic Freedom in Parton Language*. Nucl. Phys. B 126, 298-318 (1977).

[10] E.A. Kuraev, L.N. Lipatov, V. S. Fadin *The Pomeranchuk Singularity in Nonabelian Gauge Theories*. Sov. Phys. JETP 45, 199-204 (1977).

[11] E.A. Kuraev, L.N. Lipatov, V. S. Fadin *Multi - Reggeon Processes in the Yang-Mills Theory*. Sov. Phys. JETP 44, 443-450 (1976).

[12] I.I. Balitsky, L.N. Lipatov *The Pomeranchuk Singularity in Quantum Chromodynamics*. Sov. J. Nucl. Phys. 28, 822-829 (1978).

[13] I. Balitsky *Operator expansion for high-energy scattering*. Nucl. Phys. B 463, 99-160 (1996).

[14] Y.V. Kovchegov *Small x F_2 structure function of a nucleus including multiple pomeron exchanges*. Phys. Rev. D 60, 034008 (1999).

[15] Y.V. Kovchegov *Unitarization of the BFKL pomeron on a nucleus*. Phys. Rev. D 61, 074018 (2000).

[16] J. Jalilian-Marian, A. Kovner, L. McLerran, H. Weigert *Intrinsic glue distribution at very small x*. Phys. Rev. D 55,5414-5428 (1997).

[17] J. Jalilian-Marian, A. Kovner, A. Leonidov, H. Weigert *The BFKL equation from the Wilson renormalization group*. Nucl. Phys. B 504, 415-431 (1997).

[18] J. Jalilian-Marian, A. Kovner, A. Leonidov, H. Weigert *The Wilson renormalization group for low x physics: Towards the high density regime*. Phys. Rev. D 59, 014014 (1998).

[19] J.E. Iancu, A. Leonidov, L. McLerran *Nonlinear Gluon Evolution in the Color Glass Condensate: I*. Nucl. Phys. A 692, 583-645 (2001).

[20] S. Donnachie, G. Dosch, P. Landshoff, O. Nachtmann *Pomeron Physics and QCD* . Cambridge University Press (2002) ISBN 052178039X

[21] H. Kowalski, L. Motyka and G. Watt *Exclusive diffractive processes at HERA within the dipole picture*. Phys.Rev.D74:074016 (2006)

[22] A.G. Shuvaev, K.J. Golec-Biernat, A.D. Martin, M.G. Ryskin *Off-diagonal distributions fixed by diagonal partons at small x and xi*. Phys. Rev. D60 (1999)

[23] H. Kowalski, D. Teaney *An Impact Parameter Dipole Saturation Model*. Phys. Rev. D 68, 114005 (2003)

[24] J.Nemchik, N.N. Nikolaev, B.G. Zakharov *Scanning the BFKL pomeron in elastic production of vector mesons at HERA*. Phys.Lett. B341 (1994)

[25] J.Nemchik, N.N.Nikolaev, E.Predazzi, B.G.Zakharov *Color dipole phenomenology of diffractive electroproduction of light vector mesons at HERA*. Z.Phys. C75 (1997)

[26] J. R. Forshaw, R. Sandapen, G. Shaw *Colour dipoles and rho, phi electroproduction*. Phys.Rev.D69:094013 (2004)

[27] K. Golec-Biernat, M. Wüsthof *Saturation Effects in Deep Inelastic Scattering at low Q^2 and its Implications on Diffraction*. Phys.Rev.D59:014017 (1998)

[28] K. Golec-Biernat, M. Wüsthof *Saturation in Diffractive Deep Inelastic Scattering*. Phys.Rev.D60:114023 (1999)

[29] J. Cepila, J.G. Contreras, J.D. Tapia Takaki *Energy dependence of dissociative J/ψ photoproduction as a signature of gluon saturation at the LHC*. Phys.Lett. B766 (2017)

[30] J. Cepila, J.G. Contreras, M. Krelina, J.D. Tapia Takaki *Mass dependence of vector meson photoproduction off protons and nuclei within the energy-dependent hot-spot model*. Nucl.Phys.B 934 330-340 (2018)

[31] D. Bendová *Study of hadron structure within quantum chromodynamics*. Diplomová práce, ČVUT, Praha (2018)

[32] D. Bendova, J. Cepila, and J.G. Contreras *Dissociative production of vector mesons at electron-ion colliders*. Phys. Rev. D 99, 034025 (2019)

[33] R.L. Burden, J.D. Faires, A.M. Burden *Numerical Analysis*. ISBN:9781305253667 (2016)

[34] H1 Collaboration *Elastic J/ψ production at HERA*. Eur. Phys. J. C 46, 585–603 (2006)

[35] ZEUS Collaboration, S. Chekanov et al. *Exclusive electroproduction of ϕ mesons at HERA*. Nucl.Phys.B718:3-31 (2005)

[36] H1 Collaboration, F.D. Aaron et al. *Diffractive Electroproduction of rho and phi Mesons at HERA*. JHEP 05 (2010)

[37] H1 Collaboration, S. Aid et al. *Elastic photoproduction of ρ^0 mesons at HERA*. Nucl.Phys.B 463 3-32, (1996)

[38] ZEUS Collaboration, J. Breitweg et al. *Exclusive electroproduction of ρ^0 and J/ψ mesons at HERA*. The European Physical Journal C - Particles and Fields volume 6, 603–627 (1999)

[39] ZEUS Collaboration, S. Chekanov, et al. *Exclusive ρ^0 production in deep inelastic scattering at HERA*. PMC Phys. A1:6 (2007)

[40] H1 Collaboration, C. Alexa et al. *Elastic and Proton-Dissociative Photoproduction of J/psi Mesons at HERA*. Eur. Phys. J.C 73 (2013)

[41] H1 Collaboration, C. Adloff et al. *Elastic photoproduction of J / psi and Upsilon mesons at HERA*. Phys.Lett.B 483 (2000)

[42] ZEUS Collaboration, S. Chekanov et al. *Exclusive photoproduction of upsilon mesons at HERA*. Phys.Lett.B 680 (2009)

[43] LHCb Collaboration, R. Aaij et al. *Measurement of the exclusive Υ production cross-section in pp collisions at $\sqrt{s} = 7$ TeV and 8 TeV*. JHEP 09 (2015)

[44] CMS Collaboration, A. M. Sirunyan et al. *Measurement of the exclusive Υ production from protons in pPb collisions at $\sqrt{s_{NN}} = 5.02$ TeV*. Eur. Phys. J.C 79 (2019)

[45] ALICE Collaboration, B. Abelev et al. *Exclusive J/ψ Photoproduction off Protons in Ultraperipheral p-Pb Collisions at $\sqrt{s_{NN}} = 5.02$ TeV*. Phys. Rev. Lett. 113, 232504 (2014)

[46] ALICE Collaboration, S. Acharya et al. *Energy dependence of exclusive J/ψ photoproduction off protons in ultra-peripheral p-Pb collisions at $\sqrt{s_{NN}} = 5.02$ TeV*. Eur.Phys.J.C 79 (2019)